



Feasibility of Using Phone and Web Cameras to Detect Micro-Expressions for Lie Detection

Lanz Kendall Lim, Eden Paige Ong, Carl Arjan Ramos,
Mico Dellosa, and Fritz Kevin Flores
St. Edward School, General Trias City, Cavite

Abstract: This study explores the feasibility of using low-resolution cameras as a means of detecting facial movements for lie detection. Micro-expressions, however, are difficult to detect by the human eye due to their short duration and low intensity, thus the research explores the possibility of extracting micro-expressions from phone or web cameras that have low resolution and framerate. The collected videos are the processed using time series processing, to obtain both facial data points extracted from facial landmark detection models, as well as image generation from the obtained datapoints to produce a face structure. The classification mainly focuses on the use of common machine learning algorithms, to detect facial movement patterns, in the hopes of classifying people telling truths or lies. The tests ultimately proved to have a low accuracy in classification, but the results show that the methodology may contribute to other domains, such as in person identification, as well as possible recommendations for future works.

Key Words: Facial Landmarks, Image Transform, Machine Learning, Time Series.

1. INTRODUCTION

People have the innate ability to make facial expressions. Feelings of joy, sadness, anger, fear, etc., are expressed on faces via what is commonly interpreted as macro-expressions; however, there are also unseen movements in the face, known as micro-expressions. According to Ekman and Friesen (1969), micro-expressions are involuntary emotional responses that can be used to reveal one's true emotions and claimed that micro-expressions might be the most promising approach to detecting lies; however, micro-expressions are imperceptible to the untrained eye due to their short duration, with an upper limit of 0.5s, and low intensity. Zhang et al. (2014) described that micro-expressions are linked to the flow of expressions and occur unconsciously when emotions are concealed or repressed, expressing certain movement patterns which may aid in identifying individuals telling the truth or lies. Experts would classify micro-expressions according to the emotion being manifested, which is both tedious and time consuming.

Face detection programs have since then been investigated as a means of perceiving micro-expressions. Researchers use high-resolution cameras with framerates of 120 fps or above, to see subtle movements; however, these cameras tend to be expensive and are not always accessible. The study aims to investigate the feasibility of using low-resolution and low-framerate cameras as a means of capturing micro-expressions and facial patterns to classifying truth or lies.

2. Methodology

The methodology is comprised of the Preparation and Data Collection, Facial Landmark Detection and Preprocessing, and Image Generation and Time Series Processing phases.

2.1. Preparation and Data Collection

During this phase, participants undergo an Emotional Intelligence (also known as EQ) Test, to determine if the participant is capable of understanding and managing ones emotions, which may relate to a degree of emotional expressiveness and is used to determine eligibility for participation. This allows selected participants who are generally able to better express emotions, to participate in the study, in the hopes of being able to obtain more descriptive data for processing.

The fifteen selected participants are then oriented regarding the study and requested their consent for participation. They then proceeded to a recorded online interview, comprised of twenty (20) yes-or-no questions, of which they have the option to tell the truth or lie. At the end of the video, the participants are requested to label their answers, to serve as the ground truth.

Each video recording of the online interviews uses 60 fps and is processed by splitting the video per question, and further trimming each one by only retaining the segments where the participants answered. These video segments, containing the participants providing yes-or-no answers, are then

labelled indicating if they are truth or lie, then are sent to the next phase.

2.1. Facial Landmark Detection and Preprocessing

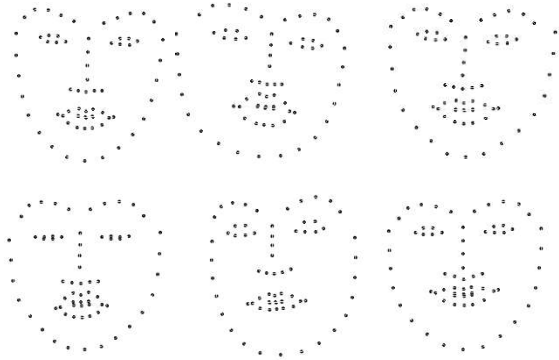


Figure 1. Samples of Facial Landmark Annotation from Video Segment Frames

The labelled video segments are run through a feature extraction algorithm using computer vision and image processing. The process begins by splicing the video segments into individual frames, allowing each frame to be subjected to the facial landmark extraction algorithm. The algorithm enables detection and extraction of sixty-eight (68) facial landmarks from each frame in as presented in Figure 1. This also determines the location of the whole face in the entire frame.

Since different participants are positioned differently in the frame and do not have a constant position across different video segments, even within the same interview, additional preprocessing was implemented. For each video segment, the size of the face relative to the chin and eyebrows, as well as the position of the face relative to the nose, were used as guidelines to perform affine transformation methods of scaling and translation respectively, and in addition, the images were also scaled to an arbitrary 1000px by 1000px image size. This is to normalize the size and position of the faces, across each video segment, for use of processing in the study.

2.2 Image Generation and Time Series Processing

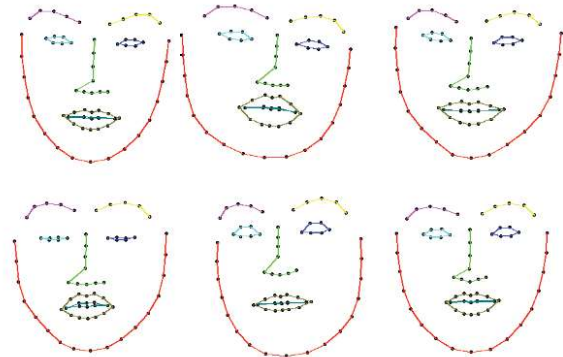


Figure 2. Samples of Facial Landmark Annotation with Facial Feature Annotation

The transformed facial landmark points from the video segments are then processed further to generate two datasets: the image dataset and time series dataset. The image dataset begins by annotating the facial landmark points by using colored lines to connect certain facial features, as seen in Figure 2. The colors and lines are assumed to be useful in processing, by guiding the machine learning algorithms of the different facial features, identified by a unique color scheme.

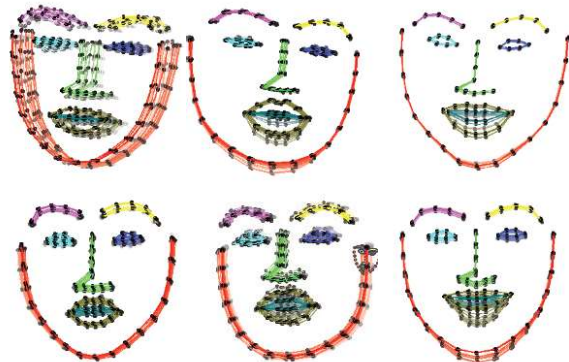


Figure 3. Samples of Facial Movement Annotation with Alpha Adjustment with Respect to Time

Since each video segment is a series of frames, an additional temporal aspect needs to be included, expressing information from the start frame to the end frame of each video segment. Therefore, the solution was to annotate all frames, but have a gradual increase of transparency from 0% to 100%, to represent a gradual transition from transparent to opaque, representing time.

Table 1. Subset from the Initial Facial Landmark Dataset from Feature Extraction

label	participantID	testNum	frameNum	jaw0-x	jaw0-y	jaw1-x	jaw1-y	jaw2-x	jaw2-y
L	0	1	1	714	452	715	503	721	552
L	0	1	2	742	427	742	475	747	521
L	0	1	3	773	439	773	487	776	532

The time series dataset on the other hand, was processed from the initial facial landmark points, containing both x-axis and y-axis for each of the 68 points, with a total of 136 features. Unfortunately, each video segment contains varying number of frames (rows), due to the participants having various durations in providing answers, thus requiring time series processing, to represent the entire sample in only a single row. The algorithm implemented to address the concern was to implement a MinMaxAve Scaling for time intervals with overlap.

The time interval used in the study was to split the video segment into three (3) equal parts, indicating the start, middle, and end of an answer, by dividing the number of frames into three (3) groups. An overlap between the start-middle and middle-end were also obtained using the same number of frames used on the split, creating a total of five (5) subsegments. Each subsegment contained the 136 features from the facial landmark points, and is further processed to get the minimum, maximum, and average of each subsegment, reaching a total of 2040 feature columns per sample. The entire dataset is then normalized using MinMax Scaler for machine learning.

3. TEST RESULTS AND DISCUSSIONS

The time series dataset was investigated using Support Vector Classifier and Linear Regression algorithms to determine its ability to classify the data between truth or lie.

Table 2. Support Vector Classifier Result

Label	Precision	Recall	F1-Score	Support
0 – Lie	50%	25%	33%	12
1 – True	62%	83%	71%	18
Accuracy			60%	30

Using different Train-Test proportions, the best result was obtained using a proportion of 90% train and 10% test. Hyperparameter tuning includes a grid search of the following values: C of 0.01, 0.1, 1, or 10; gamma of 0.1, 0.01, or 0.001; and kernel of rbf, poly, sigmoid, or linear; having the best hyperparameters with C=10, gamma=0.1, and kernel=linear. Unfortunately, with all tests implemented, the accuracy ranged from 47% to 60%, with the highest shown in Table 2 for Support Vector Classifier. Logistic Regression results ranges from 49% to 56%. This means that the classifiers have

difficulty in determining the difference of true and lie from the dataset.

Another investigation was done by performing algorithms in dimensionality reduction via Principal Component Analysis to simplify the dataset features. Additionally, K-Means clustering was performed in order to determine if the clusters are able to distinguish some differences.

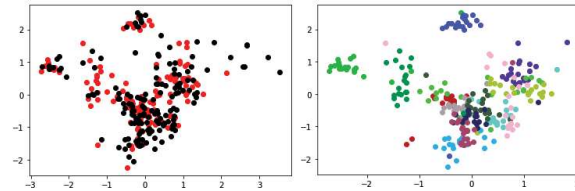


Figure 4. PCA Visualization for Truth and Lies (left) and by Participant (right)

Figure 4 present the results obtained from the PCA Visualization. The left figure uses Red points to denote lie samples and Black points for truth samples. It can be seen that there is not much differences with the truth and lie samples, hence the low accuracy obtained by the Support Vector Classifier and Logistic Regression algorithms. However, even though the images were already normalized through transformations in translation and scaling, figure on the right of Figure 4, presenting a unique point color per participant, still indicated visually observable grouping and clusters for each individual, indicating a similarity in the individuals data despite normalization.

This indicates the possibility that the methodology implemented in the study can, in a way, have the capability for other implementations, such as to identify a participant or individual from the rest, only through the use of the facial landmarks and facial movement of the individual.

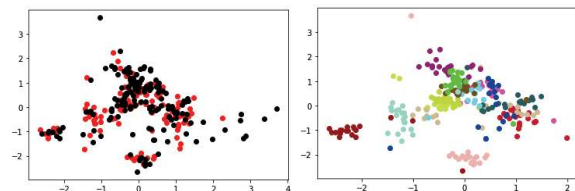


Figure 5. PCA with StandardScaler Visualization for Truth and Lies (left) and by Participant (right)

Additional testing of the hypothesis that the methodology can be used for studies in identification was implemented by implementing PCA one again, but this time, processing the data using Standard Scaling. The result in Figure 5, reveals a result that is somewhat similar to that of Figure 4, where the left image has some difficulty in identifying truth from lie samples, but the image on the right, still shows some form of clustering per participant.

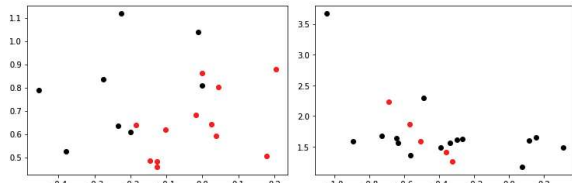


Figure 6. Sample PCA Visualization per Participant showing Visual Differences

Further observing the visualizations with regards to the individual participant data can be seen in Figure 6. The left image, obtained from one participant, seems show that there is a visually observable separation from the truth (black points) and lie (red points) samples of the participant. This could indicate quantitative evidence that the micro-expressions of an individual, when lying, is specific to that individual. This also merits further investigation on user-dependent and user-fold validation techniques as recommendation for future researchers.

4. CONCLUSION

The study performed various techniques from extracting facial landmark points from video frames, performing affine transformation methods of scaling and translation to provide uniformity to the data, implementation of time series processing via MinMaxAve scaling for time intervals with overlap due to the temporal aspect of the data, generate facial feature visualizations representing time using changes in transparency, as well as implementation of basic machine learning algorithms for classifications. Although the accuracy obtained in the study did not exceed 60%, even with simple binary classification, other results show some opportunity for improvement as well as use of the methodology in different applications. With limited dataset and resources, the study is still at its early stages, and more improvement can be made, such as normalizing the samples since the number of truth and lie samples in the data collection is uneven; further transformation of rotation and scaling for the images, since some participants tend to rotate and angle their faces; implementation of Convolutional Neural Network and other Deep Learning algorithms instead of simply using visual observation, and others.

5. REFERENCES

Agrawal , S., & Khatri, P. (2015). Facial Expression Detection Techniques: Based on Viola and Jones algorithm and Principal Component Analysis. 2015 Fifth International Conference on Advanced Computing & Communication Technologies, (pp. 108-112). Haryana. doi:10.1109/ACCT.2015.32

Ekman, P., & Friesen, W. V. (1969). Nonverbal Leakage and Clues to Deception. *Psychiatry: Journal for the Study of Interpersonal Processes*, 32(1), 88-106.

Yan, W.-J., Wang, S.-J., Liu, Y.-J., Wu, Q., & Fu, X. (2014). For micro-expression recognition: Database and suggestions. *Neurocomputing*, 136, 82-87. doi:<https://doi.org/10.1016/j.neucom.2014.01.029>

Zhang, M., Fu, Q., Chen, Y.-H., & Fu, X. (2014). Emotional Context Influences Micro-Expression Recognition. *Plos One*, 9(4). doi:10.1371/journal.pone.0095018



Developing a Prototype for a Microcontroller-Based Coin-Counting Machine

Jean Louis Lance Y. Cabrera, Daenielle D. Cruz, Bentley Andrew Y. Lu
Jorgette Courteney C. Siy, and Clement Y. Ong
De La Salle University Integrated School, Manila

Abstract: Coins have become a significant part of today's economy and are continuously being distributed, along with banknotes, for daily transactions in the most conventional methods. The modernized circulating currency method relies heavily on coin sorting and counting machines to prevent inconsistencies when handling and calculating coins. While the innovation reduces the need for human resources and revolutionizes the way establishments work with large sums of coins, accuracy in differentiating coins becomes an issue in some existing designs. The prototype uses light occlusion and measures the energy of the coin impact to identify the denomination. The prototype shows promise in being able to identify four Philippine coin denominations.

Key Words: coin denomination; coin detection; coin properties; accelerometer sensor; light dependent sensor

1. INTRODUCTION

Coins have had a significant impact on the current currency system of the Philippines. As of March 31, 2019, 31.8 billion pieces of coins valued at 39.5 billion Philippine Pesos have been produced (Bangko Sentral ng Pilipinas, 2019). The Bangko Sentral ng Pilipinas (BSP) ensures that the supply and division of coins are sufficient and non-repetitive (Chipongian, 2019). According to Doza (2018), there was a new update on the currency of the Philippines, which is called the "New Generation Currency (NGC)." The BSP made new coins having millimeters of 20, 16, 15, 23, 25, 27 for the diameters of 25-Centimo, 5-Centimo, 1-Centimo, 1-Peso, 5-Peso, and 10-Peso (Doza, 2018). These new coins have new security features, consisting of an electromagnetic signature embedded and considered (Doza, 2018; Rogers & Thomas, 2017).

As coins are highly used in the country, coin counterfeiters have constantly been trying to abuse this. There are currently two false identification systems used in coin counter machines: mechanical and technological (Delgado, n.d; Hu, n.d.). According to Hu (n.d.), mechanical coin tester mechanisms check the coin's width and weight to determine its denomination and use electromagnetism to identify its coin denomination. According to Delgado (n.d.), technological coin tester mechanisms use image capturing technology or Circular Hough Transform (CHT) to identify its authenticity as it would find all the possible radii to locate the placement of the coin. Afterward, it would utilize the Fisher Linear Discriminant analysis and electromagnetism to identify the coin denominations (Delgado, n.d.). At

present, coin counting machines are still utilizing false identification systems to increase their security and avoid counterfeit coins (Chipongian, 2019). However, according to ABS-CBN News (2017), it was not until March of 2018 when the Light Rail Manila Corporation (LRMC) updated its ticket vending machines four months after the release of the new 5-peso coin.

To solve the problem, a new prototype for a coin-counting machine was proposed. This prototype has an ingenious way of identifying Philippine coins, despite designs varying throughout the years, that are efficient, accurate, and made with quality materials to better its performance. The researchers aim to implement non-image sensing technologies to develop a software that could distinguish coin denominations such as 1-Peso, 5-Peso, 10-Peso, and 20-Peso, based on the sensor data. Coins deliberately altered (mutilated or deformed), damaged (oxidized, worn down), commemorative coins, and centavos cannot be classified or identified as acceptable. The researchers would evaluate the prototype's consistency and speed in distinguishing these various coin denominations.

The findings of this study will greatly benefit those who frequently utilize coins. This prototype serves as a guide for people to improvise ways to identify and distinguish Philippine coins. Also, establishments that usually need to input coins will have a more convenient time as determining coins of different denominations would become timesaving and better in terms of accuracy. Besides this, future researchers can further their knowledge with this prototype acting as a basis for refinement of future works.

2. METHODOLOGY

2.1 Light Dependent Sensor

This sensor consists of a light dependent resistor (LDR) and a light-emitting diode (LED) set to face each other, wherein an uploaded code will solve for the time occluded as the coin passes through (Figure 1). Ten trials were done per coin denomination. After the first ten trials, changes were made to make coin drop more consistent: the use of a coin dropper, the height drop setting (6 cm), and the use of an LM324 following a circuit diagram (Figure 2).

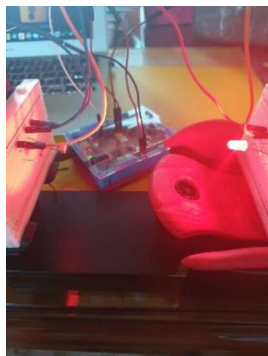


Figure 1. Initial Setup for Light Dependent Resistor.

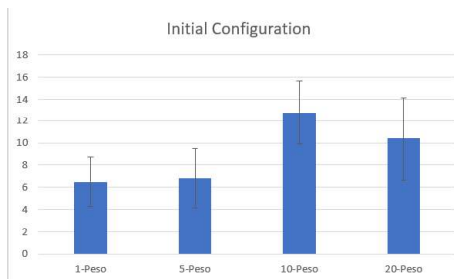


Figure 2. Initial results of Light Dependent Resistor.

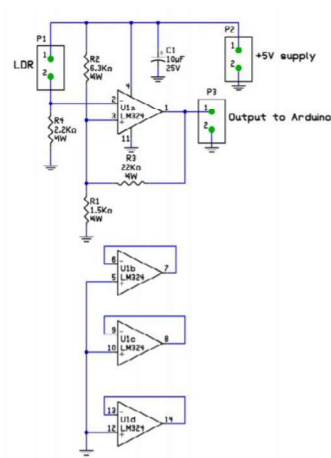


Figure 3. Circuit Diagram for Light Dependent Resistor.

2.2 ACCELEROMETER SENSOR

This MPU-6050 accelerometer is attached to a plate and anchored to two boxes. When a coin is dropped on the plate, the vibrations will be collected using an uploaded code (Figure 4). Ten trials were made per coin denomination. After the first five attempts, the setup for the MPU-6050 was modified to minimize the vibrations and absorb the initial impact made by the coin (Figure 5). The MPU-6050 remained attached to the plate in the redesigned setup — tilted to an angle and placed on the floor. Furthermore, a small chair was positioned with a red circular mark to indicate the height wherein the coin will be dropped (Figure 6).



Figure 4. Initial Configuration for Accelerometer Sensor.

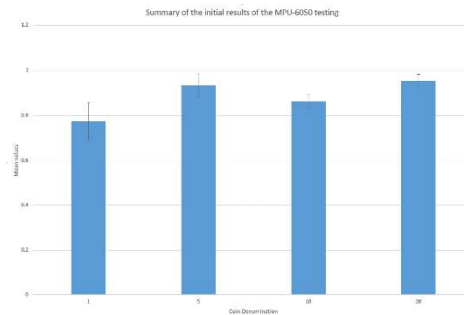


Figure 5. Summary of Initial Results of the Accelerometer Results on the Y-axis.



Figure 6. Final Configuration for the MPU-6050 Sensor.

2.3. Prototype Testing

After conducting and recording the light dependent sensor and accelerometer sensor trials, both sensors were combined into one prototype (Figure 7). Nevertheless, the prototype utilized the same height (6 cm) used for dropping the coin with a coin dropper, while the accelerometer sensor utilized the chair with a circular mark. There were slight changes to enhance the prototype's performance: the addition of another chair, cardboard (to hold the light dependent sensors), and cardboard (on top of the accelerometer sensor).



Figure 7. Prototype Setup.

3. RESULTS AND DISCUSSION

3.1. Light Dependent Sensor

After several trials and alterations, results showed gradual improvements from each adjustment made (Table 1). The light dependent sensor's initial trial had a minimum standard deviation of 2.202, which then changed to 0.539 in the final results. The mean values also went from an indistinguishable set of numbers to a distinguishable and concise set of numbers. Furthermore, coin denominations such as one and five overlapped, while denominations ten and twenty were not overlapping (Figure 8).

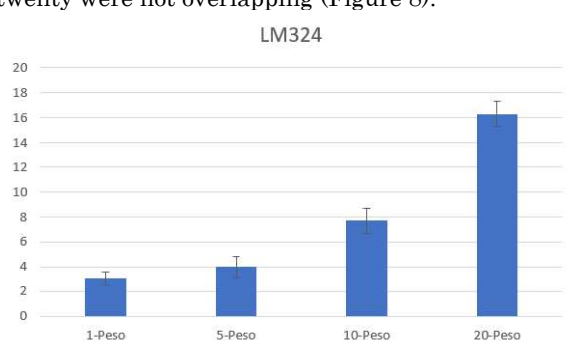


Figure 8. Final results of the light dependent sensor.

Table 1. Results of the Changes of Light Dependent Sensor

		1- Peso	5- Peso	10- Peso	20- Peso
Initial	Mean	6.5	6.8	12.8	10.4
Configuration	Standard Deviation	2.202	2.676	2.891	3.720
Addition of a ruler	Mean	5.9	8.3	10	15.8
Addition of a coin dropper	Standard Deviation	1.135	1.552	1.483	1.720
Final	Mean	10	10.6	12.2	8.2
Setup	Standard Deviation	0.755	1.114	1.400	1.077
	Mean	3.1	4	7.7	16.3
	Standard Deviation	0.539	0.831	1.00	1.00

3.2. Accelerometer sensor

Based on the final results of the MPU-6050 trials, it can be seen that the significant impact of the coin would be on the Y-axis as it is the focal point of the drop, having the values vary significantly (Table 2). However, the X and Z values differ from each denomination. These values were caused by the plastic plate's movement horizontally when impacted by the drop of the coin; therefore, the Y value was considered.

Table 2. Final Results of the MPU-6050 Testing

	Trials				
	1	2	3	4	5
1-Peso					
X	3.78	4.07	4.78	4.00	3.56
Y	0.22	-0.27	0.08	0.05	0.22
Z	-9.73	-11.42	-14.95	-10.96	-10.55
	6	7	8	9	10
X	4.35	4.26	3.75	3.75	1.26
Y	-0.07	0.06	-0.25	-0.04	-0.25
Z	-12.65	-11.96	-11.19	-10.21	-12.98
5-Peso					
X	3.44	3.20	5.97	3.77	3.11
Y	-0.22	-0.15	-0.34	0.06	-0.50
Z	-10.27	-9.47	-17.73	-11.26	-8.78
	6	7	8	9	10
X	3.91	4.20	4.77	4.30	3.09
Y	-0.10	-0.44	-0.21	-0.47	-0.33
Z	-11.33	-12.97	-11.01	-14.04	-10.21
10-Peso					
X	3.65	3.77	4.29	4.32	3.80
Y	-0.35	-0.39	-0.44	-0.54	-0.28
Z	-11.61	-10.41	-11.68	-12.51	-10.44
	6	7	8	9	10
X	4.57	6.55	4.98	3.32	4.15
Y	-0.42	-1.28	-1.36	-0.62	-1.11
Z	-12.70	-17.44	-16.54	-10.77	-15.22
20-Peso					
X	4.65	4.25	5.01	4.15	5.83
Y	-2.65	-3.58	-2.29	-1.07	-1.88
Z	-10.90	-15.35	-8.32	-11.79	-11.05
	6	7	8	9	10
X	2.68	3.56	4.50	4.47	3.46
Y	-3.32	-1.96	-1.56	-1.05	-1.26
Z	-3.65	-6.68	-10.55	-8.05	-7.53



There were more distinct and wide-spread means than the initial results; however, this could be decreased by dropping the coin in a consistent manner (Table 3 & Figure 9).

Table 3. Summary of the Final Results of the MPU-6050 Configuration

Coin	Mean	Standard Deviation
1-Peso	-0.025	0.175
5-Peso	-0.270	0.170
10-Peso	-0.679	0.388
20-Peso	-2.060	0.850

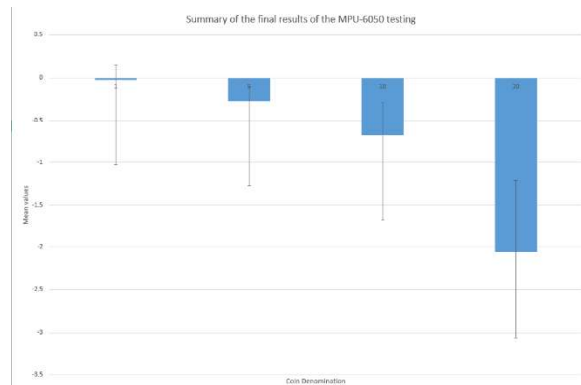


Figure 9. Summary of the Final Results of the MPU-6050 Testing.

3.3. Prototype Testing

The final results of both the light dependent sensor and the accelerometer sensor were utilized as a guide to determine the coin denomination being dropped. However, the results were not similar to the final results due to the variety of ways in coin dropping. Hence, another set of trials were conducted to obtain the sensors' data with the combined setup (Table 4). These values consisted of the time occluded by the coin, the peak value of the y-axis, and the average values around the peak of the y-axis (consists of one value before the peak, the peak itself, and three values after the peak).

Table 4. Results of Prototype Testing

	Trials					
	1-Peso	1	2	3	4	5
Time Occluded	8	8	8	8	9	
Peak Value	5.75	5.64	5.45	4.73	6.21	
Average Values around the Peak	5.43	3.19	3.32	3.30	4.22	
		6	7	8	9	10
Time Occluded	8	8	8	8	9	
Peak Value	4.61	6.30	6.15	4.68	3.77	
Average Values around the Peak	2.46	3.65	3.76	2.89	2.84	
		1	2	3	4	5

Time Occluded	9	9	10	9	10
Peak Value	6.93	7.58	9.25	7.77	9.10
Average Values around the Peak	4.04	4.79	5.59	4.77	5.79
	6	7	8	9	10
Time Occluded	10	10	10	9	11
Peak Value	9.47	7.31	8.34	6.71	9.68
Average Values around the Peak	5.27	4.64	5.59	3.85	5.88
	1	2	3	4	5
Time Occluded	12	12	13	11	13
Peak Value	9.61	7.74	7.77	7.21	9.72
Average Values around the Peak	6.28	4.40	4.82	4.55	5.99
	6	7	8	9	10
Time Occluded	12	14	13	12	12
Peak Value	7.26	8.25	9.88	7.75	8.50
Average Values around the Peak	4.44	4.36	5.97	4.92	5.08
	1	2	3	4	5
Time Occluded	16	16	16	18	15
Peak Value	11.23	11.05	18.88	11.00	11.05
Average Values around the Peak	6.48	6.86	6.09	6.68	7.34
	6	7	8	9	10
Time Occluded	16	16	18	16	18
Peak Value	12.06	10.66	11.92	14.57	12.09
Average Values around the Peak	7.27	4.77	6.09	8.54	7.86

Table 5. Summary of the Results of Prototype Testing

	1-Peso	5-Peso	10-Peso	20-Peso
Peak Value: Mean	5.3385	8.214	8.369	12.451
Peak Value: SD	0.8025	1.0454	0.9690	2.3900
Peak Value: Range	4.68 to 6.30	6.71 to 9.47	7.21 to 9.88	10.66 to 18.88
Average Values around the Peak: Mean	3.506	5.021	5.081	6.881
Average Values around the Peak: SD	0.7994	0.6807	0.6946	0.9674
Average Values around the Peak: Range	2.84 to 4.22	3.85 to 5.88	4.40 to 5.99	6.48 to 8.54
Time Occluded: Mean	8.2	9.7	12.4	16.5
Time Occluded: SD	0.4	0.6403	0.8	1.0247
Time Occluded: Range	8 to 9	9 to 11	11 to 14	15 to 18

The summary of the results had shown that the discriminants' hierarchy, from highest to lowest, is the time occlusion, then average values around the peak then peak values (Table 5). With this in mind, the values were simulated in a software that could determine coin denominations (Table 6).

Table 6. Confusion Matrix for Software Simulation

Coin	Coin Reading				
	1-Peso	5-Peso	10-Peso	20-Peso	Not Classified
1-Peso	10	0	0	0	0
5-Peso	0	9	1	0	0
10-Peso	0	0	9	0	1
20-Peso	0	0	0	10	0

Based on the values of Table 6, the simulation showed that the 1-Peso and 20-Peso simulations were correctly identified ten times.



Additionally, the 5-Peso and the 10-Peso simulation were both correctly identified nine times, having one incorrect result as the 5-Peso was recognized as a 10-Peso coin and the 10-Peso coin was not classified. Furthermore, this code was used to simulate ten more trials (Table 7).

Table 7. Confusion Matrix for the Live Simulation

Coin	Coin Reading				
	1-Peso	5-Peso	10-Peso	20-Peso	Not Classified
1-Peso	8	1	0	0	1
5-Peso	0	7	2	0	1
10-Peso	0	1	7	0	2
20-Peso	0	0	0	10	0

It is evident that the simulation can be used to identify coin denominations as it identified 20-Peso coins ten times, 10-Peso and 5-Peso seven times, and 1-Peso eight times, respectively. After further alterations in the code and the setup, the new setup and result can be seen in Figure 10 and Table 8.



Figure 10. Final Setup for the Prototype Testing.

Table 8. Confusion Matrix for the Final Setup

Coin	Coin Reading				
	1-Peso	5-Peso	10-Peso	20-Peso	Not Classified
1-Peso	100	0	0	0	0
5-Peso	0	97	0	0	3
10-Peso	0	0	100	0	0
20-Peso	0	0	0	100	0

As the results of the trials that can be seen in Table 8 improved, fake coins were tested whether they would be detected as any of the denominations. The fake coins that were used were 5 cents, 10 cents, 25 cents, 10 Malaysian sen, a washer, a bigger washer, and a button. The 5 cents, the washer, the bigger and the button were rejected by the setup mechanically. The washer and the bigger washer were wrapped with aluminum foil and were tested again to check whether it was not detected because of the whole between it. The washer was again rejected by the setup, while the bigger washer was detected but not classified as any

coin. On the other hand, the other coin samples were detected but not classified as any denomination. The result can be seen in Table 9.

Table 9. Confusion Matrix for other coin samples

Coin	Coin Reading				
	1-Peso	5-Peso	10-Peso	20-Peso	Not Classified
5-Cent	N/A	N/A	N/A	N/A	N/A
10-Cent	0	0	0	0	100
10 Malaysia Sen	0	0	0	0	100
25-Cent	0	0	0	0	100
Bigger washer wrapped in aluminum foil	0	0	0	0	100
Bigger washer Button	N/A	N/A	N/A	N/A	N/A
Washer	N/A	N/A	N/A	N/A	N/A
Washer wrapped in aluminum foil	N/A	N/A	N/A	N/A	N/A

4. CONCLUSIONS

The prototype setup can distinguish four Philippine coin denominations. Adjustments made to the sensors, electronically and in software, coupled with changes in the mechanical design and layout for the coin drop, contributed to the increasing ability of the prototype to identify the coins. The prototype setup can also distinguish real coins from fake coins.

5. REFERENCES

ABS-CBN News. (2017). LRT-1: ticket vending machines to accept new coins in March 2018.

ABS-CBN News. <https://news.abs-cbn.com/business/12/22/17/lrt-1-ticket-vending-machines-to-accept-new-coins-in-march-2018>

Bangko Sentral ng Pilipinas. (2019). Frequently asked questions [PDF FILE]. <http://www.bsp.gov.ph/downloads/Publications/FAQs/banknotes.pdf>

Chipongian, L. (2019). BSP to put coin-counting machines in groceries. Manila Bulletin. <https://business.mb.com.ph/2019/07/16/bsp-to-put-coin-counting-machines-in-groceries>

Delgado, D. (n.d.). Automatic coin and bill detection [PDF FILE]. https://web.stanford.edu/class/ee368/Project_Autumn_1617/Reports/report_delgado.pdf

Doza, E. (2018). BSP ensures security features in new coins. Philippine Information Agency. <https://pia.gov.ph/news/articles/1007048>

Hu, D. (n.d.). How a coin tester works. Report on how things work. https://web.mit.edu/2.972/www/reports/coin_tester/coin_tester.htm

Rogers, S., & Thomas, R. (2017). Detection of the security feature in the new £1 coin [PDF FILE]. <https://www.matlabexpo.com/content/dam/mathworks/mathworks-dot-com/images/events/matlabexpo/uk/2017/detection-of-security-feature-in-new-1-coin.pdf>



COVIDetect: A Desktop Application as a Diagnostic Tool for Novel Coronavirus (COVID-19) Pneumonia in Chest X-ray Images Using Convolutional Neural Network

Vincent A. Arellano, and Michael Angelo C. Tolentino

Philippine Science High School - CALABARZON Region Campus, Batangas City, Batangas

Abstract: The COVID-19 pandemic has heavily affected the well-being of people worldwide. Current diagnostic tools, like the RT-PCR, are expensive and time-consuming; thus, there is a need for cheaper and faster means of COVID-19 detection. This study proposes using a desktop application with a convolutional neural network (CNN) and visual analysis as a supplementary diagnostic tool for detecting COVID-19 pneumonia in chest X-ray images. The CNN used is a sequential Keras model that was trained and tested through eight epochs using an augmented dataset. Random data augmentation techniques applied were rotation and horizontal flipping, which increased the total images used to 13,584. Visual analysis was created using the Grad-CAM algorithm to determine patterns in chest X-ray images. These were implemented in a desktop application and evaluated by a professional pulmonologist. Results showed that the CNN achieved an average accuracy rate of 97.96% among the three classes, which was superior among related studies. The CNN also achieved a precision, recall, and F1-score of 99.67%, 99.62%, and 99.64% respectively for COVID-19 pneumonia, 99.26%, 94.83%, and 96.99% respectively for viral pneumonia, and 95.12%, 99.42%, and 97.22% respectively for normal chest X-ray images. Meanwhile, the visual analysis was also accurate, as evaluated by a professional pulmonologist, where patterns of haziness were determined. Hence, this could serve as an effective supplementary diagnostic tool for healthcare professionals for faster and more accurate diagnosis of COVID-19 and viral pneumonia patients.

Key Words: COVID-19; pneumonia; convolutional neural network; chest x-ray image; desktop application; Grad-CAM

1. INTRODUCTION

The Novel coronavirus or COVID-19 has become a global pandemic since 2020, caused by the severe acute respiratory syndrome coronavirus 2 (SARS-CoV-2) (Gunraj et al., 2020). The World Health Organization, as cited by Khan et al. (2020), stated that a patient that is positive for COVID-19 may develop symptoms such as fever and dry cough, pneumonia, multi-organ failure, chest pain, loss of speech or movement, and death upon infection.

As of the present, several testing methods are used in testing COVID-19 among the possible carriers of the virus. However, these tests can be quite inaccurate as the most used testing method which is the RT-PCR test has a sensitivity rate of 71% to 98% and a specificity rate of 98% to 100% in COVID-19 diagnosis (Agarwal et al., 2020). Hence, there is a need for faster and more efficient means for COVID-19 detection.

Recently, studies have been done to further detect and analyze COVID-19 pneumonia using deep learning through chest X-ray images. Wang et al.

(2020) suggested that chest X-rays are faster to operate than RT-PCR kits which take days to get results. The presence of X-ray machines in medical facilities adds to the availability and accessibility of the said testing method. Testing can also be done in a fixed X-ray machine instead of transporting the test kits from one location to another. However, present research on automated detection of COVID-19 pneumonia using deep learning techniques were challenged by the insufficient amount of identifiable chest X-rays since the outbreak was recent, possibly causing overfitting in some neural networks that would yield less accurate results.

Thus, this research study aimed to develop a convolutional neural network trained on an augmented dataset, implemented through a desktop application with visual analysis, as a low-cost, automatic, supplementary diagnostic tool for novel coronavirus (COVID-19) pneumonia and viral pneumonia from chest X-ray images utilizing deep learning techniques. Data augmentation will be implemented to a chest X-ray dataset to produce more

images with different variations and obtain more accurate results.

To support this, the effectiveness of the developed model in terms of accuracy, precision, sensitivity, and F1 score in detecting the COVID-19, viral pneumonia and normal chest X-Ray images was determined. Additionally, the accuracy of the developed model was compared to other existing CNN models or architectures that also detected the same diseases. A qualitative feedback on the desktop application from an expert pulmonologist was also obtained to further assess its effectiveness.

This study may be deemed significant to COVID-19 positive patients as they can have a real-time assessment of the status of COVID-19 pneumonia if they are symptomatic. Also, medical frontliners, radiologists, and specialized virology doctors, can be greatly assisted through fast and automated detection of COVID-19 pneumonia by analyzing X-ray images among possible COVID-19 positive patients. Along with this, hospitals and specialized COVID-19 facilities can be benefited from this research as automated COVID-19 pneumonia detection can be done using X-rays and computers which are readily available across most health establishments.

2. METHODOLOGY

2.1. Development of Augmented Dataset

The dataset utilized in this study is the COVID-19 Radiography Database developed by Chowdhury et al. (2020), which is made up of 1200 COVID-19 pneumonia, 1,345 viral pneumonia, and 1,341 normal chest X-ray images. To maximize the size of the dataset, data augmentation was applied using scikit-image, where two transformational techniques were utilized: rotation and horizontal flipping. Using data augmentation, overfitting is significantly reduced from image processing models (Gunraj et al., 2020). This resulted in an augmented dataset that is composed of 13,584 chest X-ray images, as seen in Table 2.1.

Table 2.1. Number of Images Before and After Data Augmentation of the Dataset.

	Number of Images Before Augmentation	Number of Images After Augmentation
COVID-19 Pneumonia	1200	4205
Viral Pneumonia	1345	4697
Normal	1341	4682
Total	3886	13,584

2.2. Development of the Convolutional Neural Network (CNN)

A sequential CNN was constructed using Keras and Tensorflow, where its architecture is seen in Figure 2.1. The chest X-ray is inputted in the model and enters the rescaling layer, where its dimension is resized to 256 x 256. Afterward, it undergoes 3 repetitions of a convolutional layer and a max-pooling layer. A convolutional layer extracts the features from the images. Meanwhile, a max-pooling layer attains the maximum element from the feature map extracted by the convolutional layer. Lastly, it undergoes two dense or fully connected layers, which takes the output of the previous layers, then flattens and converts them into a single vector. The probability for each class is then calculated.

After constructing the convolutional neural network, the model ran through eight epochs for training and testing. 80% of the dataset was utilized for training the model, while the remaining 20% was utilized for testing the model.

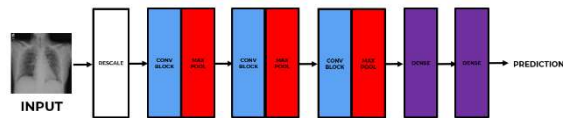


Figure 2.1. CNN Architecture of the Model

2.3. Development of the Desktop Application with Visual Analysis

The developed CNN was implemented through a desktop application using Tkinter. The user interface, as seen in Figure 2.2, shows the draft of the elements of the desktop application. The “Upload Chest X-ray Image” button allows users to upload chest X-ray images to be classified among the three groups. Once uploaded, the image would be seen in the left region, while a visual analysis using Gradient-weighted Class Activation Mapping (Grad-CAM) is provided on the right. The results of the classification would be provided at the classification label at the bottom side of the application.

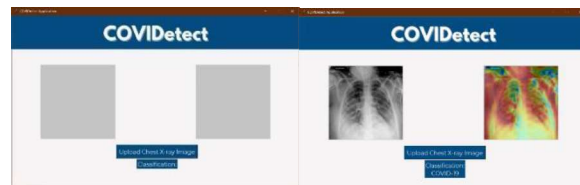


Figure 2.2. General User Interface of the Desktop Application

2.4. CNN and Desktop Application Evaluation

To assess the performance of the convolutional neural network, the following specific



metrics were obtained: True Positives (TP), True Negatives (TN), False Positives (FP), and False Negatives (FN). These were visualized using a confusion matrix, which showed the true values of the specific metrics by arranging the data in terms of its classification.

Afterward, the following performance metrics were calculated: accuracy, precision, sensitivity and F1 score. These performance metrics assess the performance and effectiveness of the developed model in classifying the chest X-ray images. The formulas for these performance metrics are:

$$\text{Accuracy} = (\text{TP} + \text{TN}) / (\text{TP} + \text{TN} + \text{FP} + \text{FN})$$

$$\text{Precision} = \text{TP} / (\text{TP} + \text{FP})$$

$$\text{Recall} = \text{TP} / (\text{TP} + \text{FN})$$

$$\text{F1 Score} = 2 \times (\text{Recall} \times \text{Precision}) / (\text{Recall} + \text{Precision})$$

The average accuracy of the model was then compared to the average accuracy of other studies that classify the same groups.

Meanwhile, to assess the performance of the desktop application, a professional pulmonologist tested the application and evaluated it through an interview.

3. RESULTS AND DISCUSSION

The confusion matrix in Table 3.1 showed that the model predicted most chest X-ray images correctly. Therefore, it could be said that the developed model is successful in classifying these images efficiently since convolutional neural networks have the property of extracting similar features or patterns in the chest X-ray images (Khan et al., 2020). The convolutional layers in the model serve as successive filters in detecting significant features in an image. Meanwhile, max-pooling layers reduce the complexity of the image by returning only the maximum value of sub-regions in the image. Lastly, fully connected or dense layers are connected to previous layers and flatten the previous output to convert it into a single vector (Albawi et al., 2018).

Table 3.1. Confusion Matrix Result of COVIDetect in Classifying COVID19, Viral Pneumonia, and Normal Chest X-ray Images

		Predicted Value		
		COVID19	Viral Pneumonia	Normal
True Value	COVID19	4189	8	8
	Viral Pneumonia	12	4454	231
	Normal	2	25	4655

■ Correctly Classified Images
 ■ Misclassified Images

Overall, it has been observed that the convolutional neural network performed efficiently in classifying these images, where performance metrics obtained were above 90% for all classifications as seen in Table 4.2.

Table 4.2. Performance Metrics of the CNN in Classifying COVID-19, Viral Pneumonia, and Normal Chest X-ray Images

Class	Precision / Specificity	Recall / Sensitivity	F1 score	Average Accuracy
COVID-19	99.67%	99.62%	99.64%	97.96%
Viral Pneumonia	99.26%	94.83%	96.99%	
Normal	95.12%	99.42%	97.22%	

The high precision rate of 99.67% for COVID-19 is essential since this indicates that there would be fewer false-positive cases of misclassified COVID-19 diagnosis. Meanwhile, the high recall rate of 99.62% for COVID-19 is also necessary since this indicates that there would be less false-negative diagnosis of COVID-19. Decreasing the chances of these types of misdiagnosis would further decrease the spread of the COVID-19 virus in the community through immediate and proper detection (Wang et al, 2020). Meanwhile, high performance metrics were also obtained by the convolutional neural network for viral pneumonia and normal chest X-ray images, implying that it would also be less likely to misdiagnose normal patients and those with viral pneumonia.

The average accuracy of the developed model was then compared to related studies that detect the same classifications, as seen in Table 4.3. It has been observed that the results obtained by the model were relatively higher compared to other studies that detect the same three classes.

Table 4.3. Comparison of Average Accuracy with Other Related Studies

Study	Architecture	Average Accuracy for Three Classes (%)
COVIDetect	Keras	97.96%
Apostolopoulos et al.	Sequential VGG-19	93.48%
Wang et al.	COVID-Net	93.3%
Apostolopoulos et al.	MobileNet v2	92.85%
Apostolopoulos et al.	Inception	92.85%
Apostolopoulos et al.	Xception	92.85%
Apostolopoulos et al.	Inception ResNet v2	92.85%
Khan et al.	CoroNet	89.60%

Despite using a simpler convolutional neural network, the obtained average accuracy in detecting



the three classes was the highest among related models. This is possibly caused by the sequential neural network being trained on an augmented dataset.

Related studies face the challenge of using an insufficient number of COVID-19 chest X-ray images due to limited data available since the pandemic was recent. It could be observed that most studies that attained a relatively lower average accuracy used fewer images for training and testing their models. Apostolopoulos et al. (2020) made use of 305 COVID-19, 2780 pneumonia, and 1583 normal chest X-ray images for the use of 4 of their model architectures that attained 93.48% for VGG-19 and 92.85% for MobileNet v2. Meanwhile, Khan et al. (2020) made use of 290 COVID-19, 327 viral pneumonia, and 310 normal chest X-ray images.

Through using data augmentation and developing an augmented dataset, this limitation is resolved. In a study by Wang & Perez (2017), they explored the use of data augmentation in the field of deep learning. Models that made use of small datasets often encounter overfitting since these do not generalize data well. Through data augmentation, more data is generated from the training data for an algorithm to perform better.

Through an evaluation of the COVIDetect desktop application by a professional pulmonologist, he stated that it accurately classifies COVID-19 and viral pneumonia, while there were minor misclassifications for normal chest X-ray images where these were misidentified as viral pneumonia. These misclassifications could be attributed to the haziness present in some normal chest X-ray images that were similar to those with viral pneumonia. Meanwhile, the visual analysis using Grad-CAM was also evaluated as accurate since the red spots effectively cover affected areas or areas with haziness.

Asides from the features of the desktop application, its usability and design were also assessed, and the professional pulmonologist stated that the application was simple, practical, and easy to use. He recommends adding the personal details of patients such as name and age, as well as including bacterial pneumonia in the application's classification.

4. CONCLUSION

Based on the gathered results and findings of the study, the following conclusions were drawn. First, the developed model achieved an average accuracy of 97.96% for detecting COVID-19 pneumonia, viral pneumonia, and normal chest X-ray images. Specifically, it achieved a precision, recall, and F1-score of 99.67%, 99.62%, 99.64% respectively for COVID-19 pneumonia, 99.26%, 94.83%, 96.99%

respectively for viral pneumonia, and 99.26%, 94.83%, 96.99% respectively for normal chest X-ray images. Second, the developed model achieved the highest average accuracy compared to other related studies that detect the same classifications, mainly attributed to the CNN being trained on an augmented dataset. Lastly, the COVIDetect desktop application was evaluated by a professional pulmonologist and its CNN was assessed as accurate with minor misclassifications, while its visual analysis was also assessed as accurate since it effectively covers all affected areas with haziness. The application was also determined to be simple, practical, and easy to use.

Future studies might consider using different architectures for the construction of their CNN. It is also recommended to further expand the scope of the study by including bacterial pneumonia classification and detection of other COVID-19 variants such as the UK variant and P3 variant. Future researchers might also determine the severity of COVID-19 present in the chest X-ray images so people with severe COVID-19 disease can easily be diagnosed. Furthermore, other related methods which are equally available and accessible as chest X-ray image classification can be explored by future researchers. The study can also be improved once more training data are publicly available.

5. ACKNOWLEDGEMENTS

The researchers wish to extend their deepest gratitude and utmost appreciation and recognition to the following persons and institutions who have helped us in the finalization and completion of this research manuscript.

Dr. Allen Roxas, an expert pulmonologist at Mary Mediatrix Medical Center (MMMC) in Lipa City, for his valuable clarifications, insights, suggestions, recommendations, and additional knowledge that he has provided us during the interview with him as part of our methodology. The researchers are also grateful for him because of his accommodation and help in fulfilling one part of our methodology.

Ms. Amy U. Aclan, research adviser of the researchers, for her honest remarks and criticisms on the study that inspired the researchers to improve the desktop application and the research paper, and for her patience in checking and reviewing our manuscript throughout the research process.

Mrs. Cladys M. Falcunaya, research teacher of the researchers, for her consistent emotional support and constructive criticisms and suggestions regarding the study that helped the researchers to pursue this research study on a higher note.

Mr. and Mrs. Vicente and Imelda Arellano and Mr. and Mrs. Mon and Noemi Tolentino, the parents of the researchers, for their unending support



and encouragement to the researchers in fulfilling their research requirements and responsibilities.

And most importantly to PSHS CALABARZON Region Campus, for their provision of high-quality research facilities and professionals to work with in accomplishing all the tasks needed for the completion of the research manuscript.

6. REFERENCES

- Agarwal, N., Raheja, A., & Suri, A. (2020). Guidelines for Preoperative Testing for Neurosurgery in COVID-19 Era: Indian Viewpoint Amidst Global Practice. *World Neurosurgery*.
- Albawi, S., Mohammed, T. A., & Al-Zawi, S. (2018). Understanding of a convolutional neural network. *Proceedings of 2017 International Conference on Engineering and Technology, ICET 2017, 2018-Janua*, 1–6. doi: 10.1109/ICEngTechnol.2017.8308186
- Apostolopoulos, I. D., & Mpesiana, T. A. (2020). Covid-19: automatic detection from X-ray images utilizing transfer learning with convolutional neural networks. *Physical and Engineering Sciences in Medicine*, 43(2), 635–640. doi: 10.1007/s13246-020-00865-4
- Böger, B., Fachi, M. M., Vilhena, R. O., Cobre, A. de F., Tonin, F. S., & Pontarolo, R. (2020). Systematic review with meta-analysis of the accuracy of diagnostic tests for COVID-19. *American Journal of Infection Control*. doi:10.1016/j.ajic.2020.07.011
- Chouhan, V., Singh, S. K., Khamparia, A., Gupta, D., Tiwari, P., Moreira, C., Damaševičius, R., & de Albuquerque, V. H. C. (2020). A novel transfer learning-based approach for pneumonia detection in chest X-ray images. *Applied Sciences (Switzerland)*, 10(2). <https://doi.org/10.3390/app10020559>
- Chowdhury, M. E. H., Rahman, T., Khandakar, A., Mazhar, R., Kadir, M. A., Mahbub, Z., Islam, M. T. (2020). Can AI Help in Screening Viral and COVID-19 Pneumonia? *IEEE Access*, 8, 132665–132676. <https://doi.org/10.1109/ACCESS.2020.3010287>
- Fang, Y., Zhang, H., Xie, J., Lin, M., Ying, L., Pang, P., & Ji, W. (2020). The sensitivity of Chest CT for COVID-19: Comparison to RT-PCR. *Radiology*, 296(2). <https://doi.org/10.1148/radiol.2020200432>
- Gunraj, H., Wang, L., & Wong, A. (2020). COVIDNet-CT: A Tailored Deep Convolutional Neural Network Design for Detection of COVID-19 Cases from Chest CT Images. 1–12. Retrieved from <http://arxiv.org/abs/2009.05383>
- He, K., Zhang, X., Ren, S., & Sun, J. (2016). Identity mappings in deep residual networks. *Lecture Notes in Computer Science (Including Subseries Lecture Notes in Artificial Intelligence and Lecture Notes in Bioinformatics)*, 9908 LNCS, 630–645. https://doi.org/10.1007/978-3-319-46493-0_38
- Khan, A. I., Shah, J. L., & Bhat, M. M. (2020). CoroNet: A deep neural network for detection and diagnosis of COVID-19 from chest X-ray images. *Computer Methods and Programs in Biomedicine*, 196, 105581. <https://doi.org/10.1016/j.cmpb.2020.105581>
- Magsambol, B. (2020, May 25). FAST FACTS: What's the difference between PCR, rapid antibody tests? Retrieved November 26, 2020, from <https://www.rappler.com/newsbreak/iq/things-to-know-polymerase-chain-reaction-rapid-anti-body-tests>
- Mahmud, T., Rahman, M. A., & Fattah, S. A. (2020). CovXNet: A multi-dilation convolutional neural network for automatic COVID-19 and other pneumonia detection from chest X-ray images with transferable multi-receptive feature optimization. *Computers in Biology and Medicine*, 122(June), 103869. <https://doi.org/10.1016/j.combiomed.2020.103869>
- Rahman, T., Chowdhury, M. E. H., & Khandakar, A. (2020). Transfer Learning with Deep Convolutional Neural Network (CNN) for Pneumonia Detection Using Chest X-Ray.
- Rajpurkar, P., Irvin, J., Zhu, K., Yang, B., Mehta, H., Duan, T., Ding, D., Bagul, A., Ball, R. L., Langlotz, C., Shpanskaya, K., Lungren, M. P., & Ng, A. Y. (2017). CheXNet: Radiologist-level pneumonia detection on chest X-rays with deep learning. *ArXiv*, 3–9.
- Shibly, K. H., Dey, S. K., Islam, M. T. U., & Rahman, M. M. (2020). COVID faster R-CNN: A novel framework to Diagnose Novel Coronavirus Disease (COVID-19) in X-Ray images. *Informatics in Medicine Unlocked*, 20, 100405. <https://doi.org/10.1016/j.imu.2020.100405>
- Sirazitdinov, I., Kholiavchenko, M., Mustafaev, T., Yixuan, Y., Kuleev, R., & Ibragimov, B. (2019). Deep neural network ensemble for pneumonia localization from a large-scale chest x-ray database. *Computers and Electrical Engineering*, 78, 388–399. <https://doi.org/10.1016/j.compeleceng.2019.08.004>
- Wang, J., & Perez, L. (2017). The effectiveness of data augmentation in image classification using deep learning. *ArXiv*.
- Wang, L., Lin, Z. Q., & Wong, A. (2020). COVID-Net: a tailored deep convolutional neural network design for detection of COVID-19 cases from chest X-ray images. *Scientific Reports*, 10(1), 1–12. <https://doi.org/10.1038/s41598-020-76550-z>
- World Health Organization. Philippines: WHO Coronavirus Disease (COVID-19) Dashboard. (2020). Retrieved October 01, 2020, from <https://covid19.who.int/region/wpro/country/ph>
- World Health Organization. WHO Coronavirus Disease (COVID-19) Dashboard. (2020). Retrieved October 01, 2020, from <https://covid19.who.int/>



Design and Analysis of a Myoelectric Arm Prosthesis for Transradial Amputees working as Auto-Mechanics

Azzam Afghani P. Alonto, Christian Ericson P. Delos Santos, Aaron Randall Jardenil
and Alan Miguel Joaquin M. Ocho
De La Salle University Integrated School, Manila

Abstract: Amputees struggle to function because of the large degree of dependence they need to execute basic tasks that people could normally do. Amputees usually opt to use a prosthesis, for cosmetic and other functional reasons, which are not often made for situations with intense physical exertion such as the workplace. Thus, this study aims to create a mechanical arm prosthesis design that is occupationally suitable for transradial amputees. The device is mostly made of acrylonitrile butadiene styrene (ABS), a type of thermoplastic. A digital model of the prosthesis, divided into three subassemblies, was created via Autodesk Inventor. These then went through Finite Element Analysis in which a 400 N load was placed to simulate a pushing force. After the simulations, it was proven that the individual subassemblies can withstand the specified force with minimal displacement and without yielding which shows that larger forces could be exerted. This also shows that ABS is a suitable material for creating such assistive devices. Further study could be made by optimizing the geometry and changing the orientation of the loads.

Key Words: pwds; transradial amputees; prosthetics; assistive device; finite element analysis

1. INTRODUCTION

Currently, there are about 1.44 million people with disabilities (PWDs) in the Philippines (Philippine Statistics Authority, 2013). According to Mina (2013), 93 out of 123 persons with mobility impairment in urban areas are either underemployed, unemployed, or apart from the labor force. It is inferable based on this data that there is a substantial number of people with missing limbs in the Philippines, either congenitally or externally, who have a difficult time getting a steady source of income.

In specifically the case of upper limb amputees, there are different situations where a person would need to get an upper limb (arms, wrists, or hands) amputated. Indications include trauma beyond repair, irreparable loss of the blood supply of that limb, malignancy, severe contracture, infection, congenital deformities, burns, electrical injury, frostbite, and complications from diseases (Maduri & Akhondi, 2018). As for the causes of these indications, except for the disease and congenital related ones, some common examples would be machinery accidents, infrastructural accidents, as well as military and athletic injuries. For these patients to cope with daily life despite their limb loss, various types of prostheses were developed.

Transradial and Congenital Transradial Amputation both refer to the loss or the absence of the forearm or anything below it, including the wrist and the hand (Ovadia & Askari, 2015). The only difference

is that the former refers to an accident or an unnatural amputation caused by outside factors, and the latter refers to a birth defect. To assist people with this condition, prostheses are developed.

A prosthesis, which is an artificial device that replaces a missing body part (Strait, 2006), was designed to solve this problem and help PWDs be more financially and physically independent. Its structural integrity was analyzed through finite element analysis. ABS or acrylonitrile butadiene styrene, a thermoplastic aliphatic polyester derived from renewable sources, was the set material for the prototype. Additionally, it utilized sensors that monitor nerve activity in muscles, known as Electromyography sensors (Vigotsky et al., 2018), to aid in its functionality. The model was constructed in Autodesk Inventor and virtually tested in Autodesk Nastran In-CAD. The prosthesis design is made for a person who is a transradial or congenital transradial amputee.

2. METHODOLOGY

2.1. Prosthesis Design

The arm prosthesis was created through Autodesk Inventor, which is a computer-aided design (CAD) software that excels in manufacturing modeling. The design process was divided into two main parts: the extension, which is the main load-bearing structure, and the terminal end, which is the



tool. The extension was primarily made of ABS and its length was based on the arm dimensions of an average Filipino man. As stated in a study by Rahmann, et al. (2018), the average forearm-to-hand length for Filipinos is 44.1cm, while the average hand length is 19.8 cm. Other dimensions such as stump length, arm diameter near the elbow, and wrist diameter were based on a sample arm with dimensions 15 cm, 9 cm, and 7 cm respectively. Though there are no maximum dimensions as to how long the stump should be, the 15 cm length was chosen as it provides enough space for the other internal components of the device without surpassing the average forearm length. The aforementioned dimensions of the prosthetic were utilized for experimentation, but the design will be made adaptable when it is set for public use. This means that the dimensions of the device, particularly the forearm length and diameters, will change to enhance the cosmetic appearance of the amputee's arm and the contact of the device to the stump. Additionally, a stretchable socket and an adjustable harness will be used to cater to the varying sizes of the arm stump and circumference. However, this was not presented in the virtual model as it is not needed in the finite element analysis. Moreover, the tool (wrench) was designed to have an effective length of 49.16 cm since it mimics the effective length of the hand combined with a model car wrench of 40 cm.

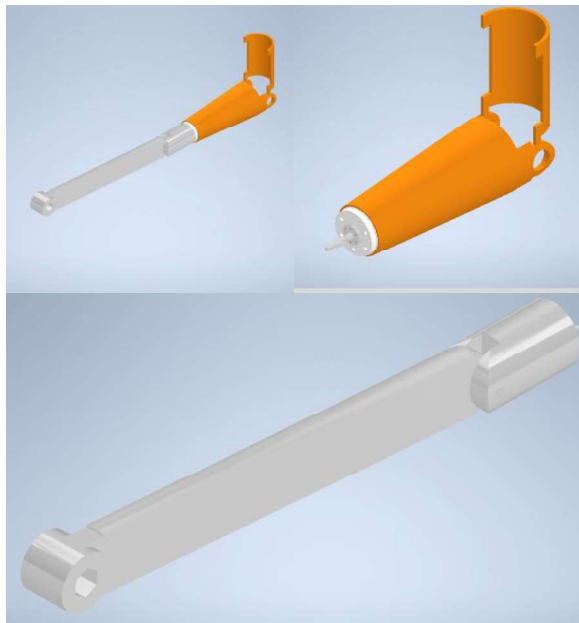


Fig 1. Full assembly of prosthetic arm (left), assembly of extension (right), assembly of sample tool (bottom)

2.2. Finite Element Analysis

The design of the prototype was only tested through virtual means with the use of Autodesk Nastran In-CAD software, which was chosen since it

is directly integrated within the modeling software. The main test involved was the linear stress tests wherein the load-bearing components of the prosthesis were analyzed by subassemblies. There are three subassemblies: the exterior shell, the motor with a shaft extension, and the sample tool, which were highlighted as orange, white, and gray in Figure 1 respectively. For each subassembly, their respective constraints, connections, and areas of load application were defined. A force of 400 N was applied as a pushing force since it is the force required to produce a torque of 145 ft/lbs when using the sample tool. The chosen torque is considered to be the maximum torque required to tighten and remove a lug nut from a car tire (Tirerack, 2021). The torquing of lug nuts is a common task in auto-mechanics, specifically in vulcanizing, hence becoming the chosen force. These loads will be applied longitudinally to simulate a pushing force to determine whether the design can tolerate the applied forces. The basis of a successful model was determined on two types of analyses: (a) von Mises stress test, and (b) safety factor. All areas of the model must retain a von Mises stress value lower than the material's stress yield. Additionally, the safety factor must verify the structural integrity of the model by providing a value greater than 1. Any unsatisfied condition would indicate that the model has yielded and must undergo modifications. These parts were not tested as a full assembly due to the limitations of the software. Further characterization is applied by analyzing displacement results.

3. RESULTS AND DISCUSSION

3.1. Analysis of Exterior Shell Subassembly

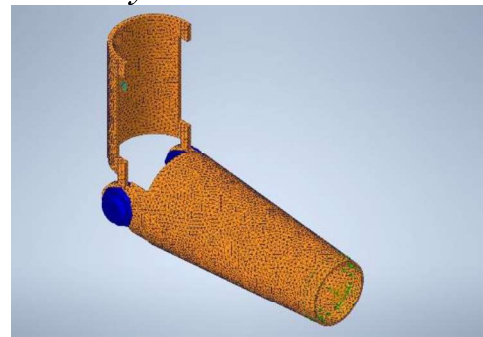


Fig 2. Specified constraints, loads, connections, and generated mesh for exterior shell subassembly

The subassembly presented in Figure 2 consists of two joined pieces wherein the vertical piece rests on the upper arm and the horizontal piece is where the stump is inserted. These two parts are joined by a bolt (presented as a blue entity in Figure 2) that is aligned with the elbow joint. The length of

the horizontal piece is 243 mm, which was achieved by obtaining the difference of the average hand-to-forearm length and average hand length as presented by Rahmann, Dawal, Yusoff, and Kamil (2018). The diameter of the hole at the rear end of the piece is 90 mm while the diameter at the front end is 70 mm. These dimensions were determined by the model arm. Additionally, the thickness of the material is consistently 5 mm thick in both components. The location and direction of the applied load are seen at the terminal end heading inward the horizontal component as represented by the green arrows in Figure 2.

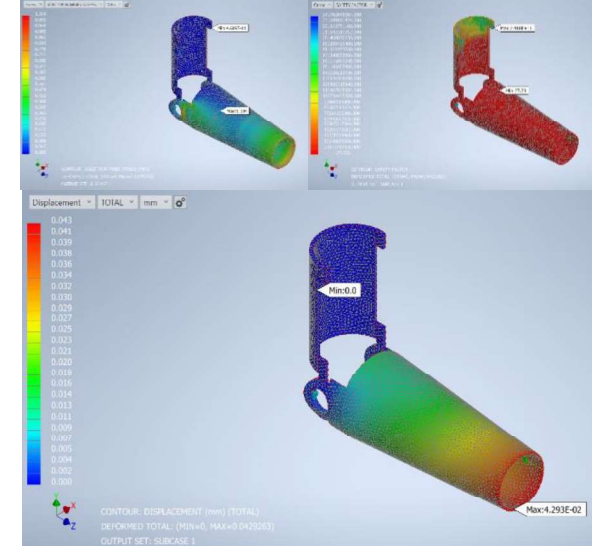


Fig 3. von Mises stress analysis (left), safety factor analysis (middle), and displacement analysis (right) of exterior shell subassembly

The material used for both components is ABS, which has a yield stress (point of shift from elastic to plastic deformation) of 20 MPa. It has a Young's modulus of 2240 and Poisson's ratio of 0.38. As seen in Figure 3, the maximum stress experienced by the model is 1.034 MPa, which is significantly lower than the yield stress. This indicates that the component would be able to withstand greater forces. Additionally, the minimum value of the safety factor analysis is far beyond 1, giving a value of 27.23. Such value would imply that the structure has no risk of yielding and is safe for use under the applied force. The displacement analysis as presented in Figure 3 shows that there is minimal deformation throughout the model. Since the maximum value, indicated by red zones in the analysis, is 0.043 mm, then it is suitable to describe that the subassembly is highly stable.

3.2. Analysis of Motor with Shaft Extension Subassembly

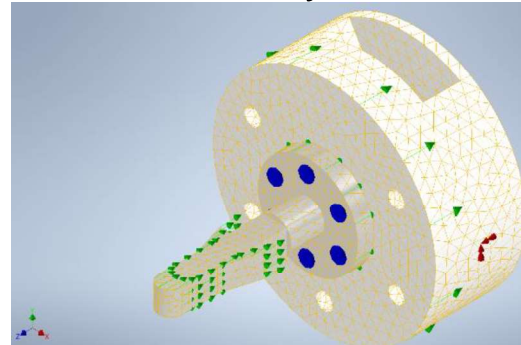


Fig 4. Specified constraints, loads, connections, and generated mesh for motor subassembly

The subassembly as presented in Figure 5 is composed of three components: (a) motor casing, (b) servo motor, and (shaft extension). The motor casing is where the servo motor fits for it to be attached to the exterior shell. Its outer surface is where the constraints are placed (as marked by the red arrows in Figure 4) due to its connection to the previous subassembly. The outer radius of the casing is 70 mm and the inner radius is 30 mm in order to fit the motor. Due to the short shaft of the motor, with a measurement of 12.4 mm, a shaft extension made of steel was added. Screws (as depicted blue in Figure 4) we used at the base of the extension to connect the extension to the shaft. Moreover, the geometry of the shaft extension is wide at half of its length so that it would serve the purpose of being part of the locking mechanism. All the components were identified to be made of steel in the finite element analysis software. The load is applied on the entire front surface as represented by the green arrows pointing towards the rear end in Figure 4.

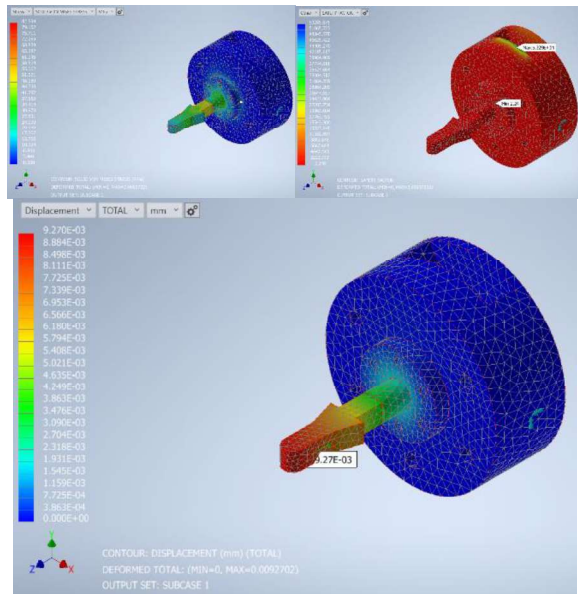


Fig 5. von Mises stress analysis (left), safety factor analysis (middle), and displacement analysis (right) of motor subassembly

With the material set to steel, its modulus of elasticity, Poisson’s ratio, and yield strength are 210000, 0.3, and 207 MPa respectively. The solid von Mises stress analysis shows that the maximum stress value is 82.594 MPa, which satisfied the first condition for the success of the subassembly. It is, however, important to observe that the area with the most stress is located at the surface of the motor, which would indicate that modifications could be made to distribute the force around the casing instead of the electrical component. Nonetheless, the current state of the model is still safe as it bears a safety factor above 1. Moreover, the displacement analysis as seen in Figure 5 shows that the force applied exerts negligible displacement since the greatest displacement experienced within the subassembly is 0.009371 mm. This would indicate that the model could handle slightly higher forces above 400 N.

3.3. Analysis of Sample Tool Subassembly

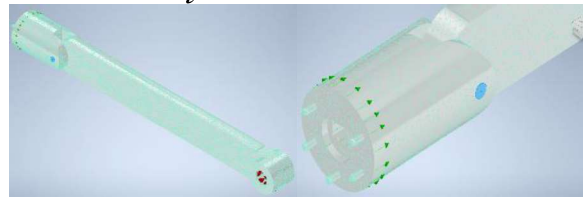


Fig 6. Specified constraints, loads, connections, and generated mesh for sample tool subassembly

The sample tool subassembly consists of three parts: (a) the rear, (b) the pin, and (c) the terminal device. The rear is the part of the tool that bears the locking mechanism which connects to the shaft extension. This is where the force is exerted as shown by the green arrows in Figure 6. It has a hole at the center where the shaft inserts and several protruding structures that connect with the holes on the motor casing. This improves the contact and load distribution between the surfaces of the subassemblies. The terminal device bears the actual tool that encloses the lug nut. The hole at the end acts as the constraint (as marked by the red arrows in Figure 6) since the lug nut is stiff prior to removing it. The two aforementioned parts are connected by a pin, which is highlighted in blue as seen in Figure 6.

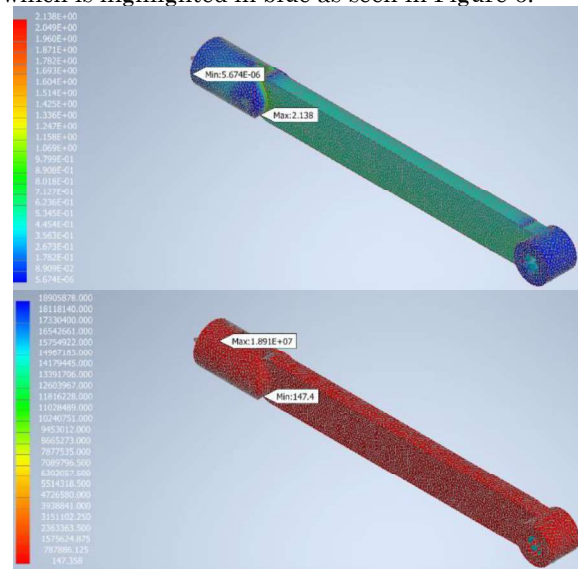


Fig 7. von Mises stress analysis (left), and safety factor analysis (right) of sample tool subassembly

All components of the sample tool are made of steel, which indicates that their Young’s modulus, Poisson’s ratio, and yield strength are 210000, 0.3, and 207 MPa respectively, similar to the specifications of the material properties in the previous subassembly.

As seen in Figure 7, the maximum stress experienced by the model is 2.138 MPa, which is significantly lower than the material's yield strength. This indicated that greater pushing forces could be exerted before the subassembly breaks. However, the concentrated area of relatively high stress at the pin indicates that further distribution of load if significantly greater forces will be applied. Though that is a reasonable observation, the minimum safety factor, which is 147.4, is also located at the pin. This shows that the model, especially the pin, can handle larger forces above 400 N since the minimum value is far beyond 1.

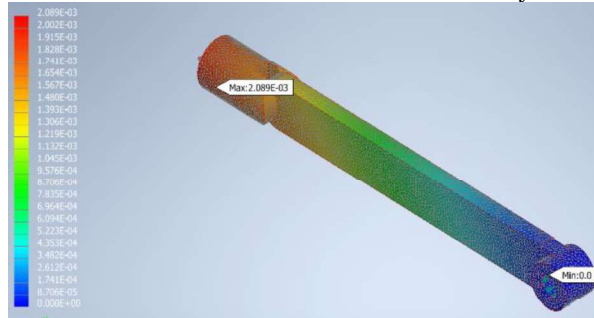


Fig 8. Displacement analysis of sample tool subassembly

The minuscule displacements presented in Figure 8 indicate that the subassembly is barely affected by the applied pushing force despite the long and slender terminal end. Though all indicators imply that the tool can handle the stress, the different angles the tool may be oriented would portray different results, which may affect the stress and displacement values of the device. Moreover, different directions of load application would also lead to varying displacement results. These situations, however, are no longer within the scope of the study but may be used for future studies.

4. CONCLUSIONS

The arm prosthesis design made for auto-mechanics is feasible since it can withstand one of the common forces exerted in car maintenance, namely the tightening and loosening of lug nuts. The individual subassemblies prove that their respective geometries and materials are able to withstand the applied force without significant displacements and yielding. Additionally, the ability of the exterior shell made of ABS to sustain the exerted force implies that it can be used as an alternative when creating arm prostheses. For further study, it is recommended to optimize the geometry of the components to disperse the load over a greater area. Additionally, different load orientations and tool orientations would be recommended to fully characterize the deformations and stress contours of the created prosthetic.

5. ACKNOWLEDGMENTS

We would like to thank our adviser Engr. Michael Manguerra for his continuous support and optimism throughout our work with this study. Even though the pandemic worsened conditions for almost everyone, he was still able to advise us properly and even help us gather our materials within the campus.

6. REFERENCES

Abd Rahman, N. I., Md Dawal, S. Z., Yusoff, N., & Mohd Kamil, N. S. (2018). Anthropometric measurements among four Asian countries in designing sitting and standing workstations. *Sādhanā*, 43(1). <https://doi.org/10.1007/s12046-017-0768-8>

Mina, C. D. (2003). Philippine Institute for Development Studies. <https://pidswebs.pids.gov.ph/ris/dps/pidsdps1313.pdf>

Ovadia, S., & Askari, M. (2015). Upper Extremity Amputations and Prosthetics. *Seminars in Plastic Surgery*, 29(01), 055–061. <https://doi.org/10.1055/s-0035-1544171>

Philippine Statistics Authority. (2013, January). *Psa.gov.ph*. <https://psa.gov.ph/content/persons-disability-philippines-results-2010-census>

Maduri, P., & Akhondi, H. (2019, May 18). Upper Limb Amputation. *Nih.gov; StatPearls Publishing*. <https://www.ncbi.nlm.nih.gov/books/NBK540962/>

Strait, E. (2006). *Prosthetics in Developing Countries*. ResearchGate; unknown. https://www.researchgate.net/publication/238088826_Prosthetics_in_Developing_Countries

Tirerack. (2021). Wheel Lug Torquing. [https://www.tirerack.com/tires/tiretech/techpage.jsp?techid=107&fbclid=IwAR1bFk5NKSWeVU7s3233G_KFhNiA3IXoacb7WxKvDiN_BdqG-cAskT_Cnko](https://www.tirerack.com/tires/tiretech/techpage.jsp?techid=107&fbclid=IwAR1bFk5NKSWeVU7s3233G_KFhNiA3IXoacb7WxKvDiN_BdqG-cAskT_Cnkohttps://www.tirerack.com/tires/tiretech/techpage.jsp?techid=107&fbclid=IwAR1bFk5NKSWeVU7s3233G_KFhNiA3IXoacb7WxKvDiN_BdqG-cAskT_Cnko)

Vigotsky, A. D., Halperin, I., Lehman, G. J., Trajano, G. S., & Vieira, T. M. (2018). Interpreting Signal Amplitudes in Surface Electromyography Studies in Sport and Rehabilitation Sciences. *Frontiers in Physiology*, 8. <https://doi.org/10.3389/fphys.2017.00985>



Prosthetic Arm for Amputees: Labor Job in Manufacturing Factories

Robyn Graesha O. Aguda, Andee Beyonce M. Co,
and Camille Elizabeth C. Reyes
De La Salle University Integrated School, Manila

Abstract: Unemployment occurs when an individual with a specified age range does not engage in work and is unpaid; furthermore, they are still looking for new job opportunities. Each person should be allowed to work and earn for their betterment, most significantly, people with physical disabilities. Most amputees utilize prostheses to resume daily tasks and adapt to a sudden lifestyle change to achieve this. This study aims to conceptualize and create a body-powered transradial prosthesis designed to execute both functions of picking and placing actions, particularly for inspection in manufacturing labor, to aid the pressure of restoring a once normal lifestyle. Upon testing the said prosthesis, it had a weight capacity of at least 20 grams with a mechanical gripper's aid to avoid slippage of the bottle. The general testing methods included 90 attempts in proving the prosthesis' functionality and weighing capacity. To conclude, it had 87% and 80% successes in terms of the primary function in both stationary and mobile trials, respectively; further, the prosthesis succeeded in carrying bottles of varying weight with an overall rate of 87%.

Key Words: prosthesis; body-powered; transradial amputee; Bowden cable; mechanical gripper

1. INTRODUCTION

According to research conducted by Mina (2013), the majority of the persons with disabilities (PWDs) in both rural and urban areas are under vulnerable employment, with only 57.1% of the total population employed. Further, several PWDs in paid employment are victims of temporary employment. With this, the government decided to establish the Republic Act No. 7277 or the Magna Carta for Disabled Persons, which took effect in 1992. This act ensures equal opportunities for suitable employment to PWDs as their able-bodied counterparts (Mina, 2013).

An amputee is considered to have a permanent total disability in the upper extremities if two limbs are lost. The loss of a finger, hand, or arm is stated to be a permanent partial disability, automatically making amputees' PWD', which affects their employment status (Labor Code of the Philippines, 2013).

Body-powered (BP) prostheses are lightweight devices controlled by cables operated by body parts. Hook BP prostheses have two types of terminal devices: Voluntary Opening (VO), which opens with no tension from the cable, and Voluntary Closing (VC), which closed due to pressure (Berning et al., 2014). Phantom limb pain (PLP), a side effect often experienced soon after surgery, is often aided by prosthesis therapy. Guo et al. (2016) reported that many experienced the disappearance of the PLP with a prosthesis; perceptions of the missing limb have

distracted the amputee from experiencing pain. The study has also concluded that amputees have better sensory feedback (i.e., visual processing of pictures) in the dominant hand compared to the remaining undisrupted limb. Hence, BP prostheses are also helpful for amputees who lost their dominant hand. Lastly, as the prosthesis's primary function in this study is to pick and place down bottles, a BP prosthesis is better suited; they are produced at lower costs, more durable, and require less training, hence more commercially available (Carey et al., 2015).

1.1 Objectives

Transradial arm prostheses are specifically designed to replace one of the two bones that make up the forearm, running from the wrist to the elbow. This study's objectives include creating a BP transradial prosthetic arm, which opens employment opportunities in factories, specifically in the quality control department. Its primary function is to pick and place a bottle with at least 20 grams of weight without damage.

1.2. Scope and Limitations

This study focuses on making a BP prosthesis similar to Smit and Plettenburg's (2010) version, which utilizes a Bowden cable. Further, the prosthesis has a VO spring gripper with the motion of compliant grasping triggered by a cable based on the concept of Lu et al. (2019). Part of this study's objectives is to create a prosthetic arm executing with repeated



action, which sets the boundary from previous models. Further, the plastic bottle utilized for testing has the following dimensions: 20 cm height, 18.4 cm body circumference, and 10 cm neck circumference.

2. METHODOLOGY

2.1 Prosthesis Design

The first sketch of the prototype utilized a solenoid actuator and a battery pack attached to the socket with a mechanical gripper taken from a toy gripper. There was also no arm area in the prototype sketch. This idea was then scratched when the goal changed to having a mechanical BP prosthesis. The final prototype sketch was used as the basis for the final prototype. PVC pipes assembled at around a 45-degree angle to serve as the arm. The gripper was also changed to a claw mechanism to have its function specific to carrying a bottle. A harness and cable mechanism were also added to support the BP mechanism of the prosthesis.

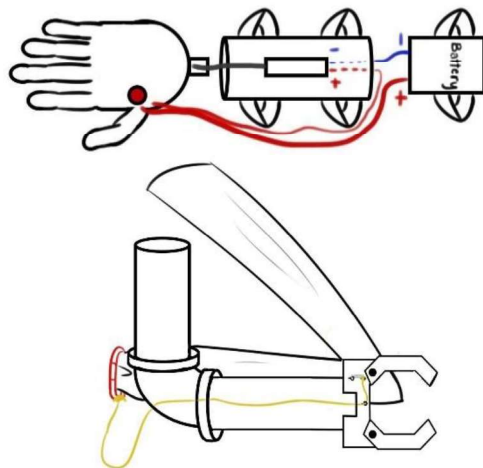


Figure 1-2. First and Final Prototype Sketch

Figure 2 showcases the prosthesis with a forearm of 45.7cm and upper arm of 23.6 cm. The prototype was initially made out of cardboard that used yarn as a cable. Measurements were adjusted before reaching the correct measurements that allowed a good grip on the bottle and were fitted to the amount of hard plastic available. The claw's final measurements were then laid out on a cutting board to be cut into the final prosthesis's gripper parts.



Figure 3-4. Cardboard Prototype of Claw Gripper and Final Prototype with Claw Gripper and Arm

The final prosthesis consists of a plastic gripper attached to the amputee's stump with a frame and a makeshift socket made of PVC pipes, as presented in Figure 5. The socket is also connected to the prosthesis's arm and a simple sash harness made of old bag straps with an adjustable buckle for the user to control their arm movement.

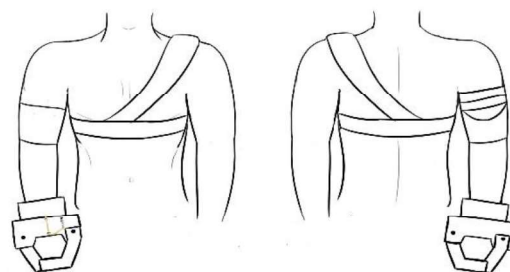


Figure 5. Front and Back View of the Prosthesis When Worn

The cable is attached to the harness's side and to the prosthetic itself, mainly to the gripper's center to pull both claws outward when the cable is stretched. Most Bowden cable prostheses have the cable placed on the arm socket's side or the harness's back. The gripper would open when the user stretches his arm and close when the arm is relaxed (Huink et al., 2016).

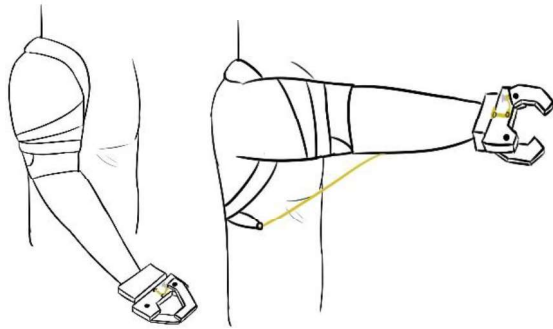


Figure 6-7. Relaxed and Stretched Position (Side View)

The standard position would have the claw closed, and the cable would pull both claw fingers, giving a broader grip that would allow the user to have a better grasp on the bottle. Figures 6-7 showcase the mentioned motion; using a Bowden cable would also reduce frequent cable tears or damage on the prosthesis (Schweitzer, 2017). Also, the prototype has a max angle of approximately 90 degrees.

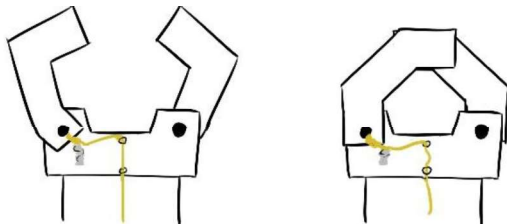


Figure 8. Gripper Design

Lu et al. (2019) utilized a shape memory alloy (SMA) actuator with a spring to control the opening and closing of a gripper. The spring used in their actuator was stretched when the gripper is opened to store elastic potential energy; with said energy, the gripper is closed as the spring locks the joints and itself back into its original position.

This concept is applied in the prosthesis' gripper design, wherein springs are attached to the same screw rings in the claw joints where the cable passes through, as presented in Figure 8. The cable passes through these screw rings and leads into the arm of the prosthesis. Each claw finger's hinge joints are screwed into the hand portion then the gripper would be attached to the prosthesis's arm. The prosthesis always remains at a curved position. The measurements are roughly 27cm for the forearm and 15cm for the upper portion of the prosthesis and socket.

2.2 Testing

The prosthesis underwent trials to test its effectiveness and if it achieves the research's objectives. Testing encompasses three stages: the first stage covered the primary function of the prosthesis;

the second involved an added distance to test its ability to carry the bottle; and the last included a slip resistance test, wherein it measures the prosthesis' capacity to carry a bottle with a weight of at least 20 grams.

The first part examined the lifting and placing ability of the prosthesis; this stage was accomplished in a stationary position and had 30 trials. While the second part involved transferring bottles from different surfaces. It tested whether the prosthesis could carry the bottle to other surfaces with a distance of one meter.



Figure 9. Experimental Setup for Lifting a Bottle

The last stage tested the prosthesis' capability to hold and sustain a bottle of at least 20 grams (minimum weight) without causing deformation. After each trial, there was an addition of 20 grams to the bottle's previous weight until it reached 200 grams. There were three trial sets for this stage, wherein each set had ten trials from the weights 20 grams to 200 grams. There was a total of 30 trials at this stage. Overall, the experimental process involved 90 trials.

2.3 Data Analysis

The first stage of testing focuses on the prosthesis' primary function: the claw's open and close movements and the ability to pick and place objects. The second part showcases the prosthesis' functionality in a factory setting. Lastly, the third stage focuses on its capacity to hold and carry a bottle with a weight of at least 20 grams until a maximum of 200 grams. According to Cooper (2019), different phases for medical equipment would equal different costs and stability of the prototype and its use.



Table 1. Prototype Development Phases (Cooper, 2019)

Phase	Qty	Cost	Time	Stability	What	Use
Appearance Model	1	\$	t	N/A	Rendered images, mock-ups	Business plan show & tell. Fundraising. Evaluation of size, color & features
Proof of Concept	1	\$\$	t	40-80%	Quick assembly of device or key parts. May not look like product	Demonstrate feasibility. Investigate risks. Select components. Investor presentation
Alpha	1-5	\$\$\$\$\$	tttt	70-90% bugs crashes	Looks-like works-like product	Test and evaluate design to find flaws. Review appearance. Limited user testing.
Beta	1-5	\$\$\$\$	ttt	90-98% almost a product	Refined Alpha prototype ready for V&V and production	Iterate & refine to make sure it meets PRS User testing. V&V testing. Clinical Trials
Pilot Production	30-100	\$\$\$	ttt	95-98% Some tooling, pcb, molding, assembly issues	Initial units assembled via production material & processes	Design transfer to production with proper QMS. Soft launch. V&V Testing. Clinical Trials
Matured Product	10k to 1M	\$\$	t	99.99%	Final product	Incorporate modifications from pilot production and clinicals. Full QMS and market release

The research focused on reaching the proof-of-concept standards since there was no actual user testing. This standard means the stability of the prosthesis should reach 40% to 80%. For a more specific standard, the research would use 80% as a benchmark on each test. Since each test would have 30 trials each, the prosthesis would need to function at least 24 out of 30 times to consider it functional and effective. Overall, the prosthesis would need to perform 72 out of 90 trials to determine its general state as a prototype.

3. RESULTS AND DISCUSSION

This study used various tests to create a voluntary opening transradial prosthesis, examine the claw's effectiveness, assess its basic functionality, and check the prosthesis weighing capacity.

The first and second stage tests the prosthesis's functionality: picking and placing a bottle; 30 trials were conducted for each stage shown in Figure 10. The first part performed the primary functions in a stationary position to see if the prosthesis can achieve the first research objective. Out

of 30 trials, the prosthesis was able to sequentially perform 26 out of 30 times or 87% of the whole time. As the prosthesis is considered a prototype, it falls under the Proof of Concept section in Cooper's Prototype Development Phases (2019.) The set functional percentage of the prosthesis is 40% to 80%, which implies it can be considered functional in the first part considering its successes.



Figure 10. Bottle Lifted by Prosthesis

The second part's trials are similar to the first, with only the addition of a measured distance of one meter to mimic quality control workers' movement in a factory setting. In all of the trials, the prosthesis sequentially acted 24 out of 30 times or 80%. With the basis of the Prototype Development Phases Table (2019), the prosthesis has exceeded the limit of 80%.

Table 2. Lifting and Placing of Prosthesis (Stationary and Mobile)

TRIAL	Lifting & Placing (Stationary)	Lifting & Placing (Mobile)
1	passed	passed
2	passed	failed
3	passed	passed
4	failed	passed
5	passed	passed
6	passed	passed
7	passed	passed
8	failed	passed
9	failed	passed
10	passed	passed
11	passed	passed
12	passed	failed
13	passed	passed
14	passed	failed
15	failed	passed
16	passed	passed
17	passed	passed
18	passed	passed
19	passed	passed
20	passed	passed
21	passed	passed
22	passed	failed
23	passed	passed
24	passed	passed
25	passed	failed
26	passed	failed
27	passed	passed
28	passed	passed
29	passed	passed
30	passed	passed



The third stage tests the prosthesis in carrying an object with a weight of at least 20 grams to 200 grams. Water was added to a plastic bottle to get the corresponding weight. In total, three sets with ten trials each were conducted to see the prosthesis's weighing capacity. Each set includes ten trials. In Table 3, the weights with asterisks imply the prosthesis started having difficulty carrying the bottle.

The first set of results showed that the prosthesis could pick up the bottle in all trials. In the second set, the prototype was able to carry eight out of ten times. In the weights 140 grams and 200 grams, it dropped the bottle during the process. In the last set, the prosthesis was also able to carry the bottle eight out of ten times. It had difficulty in maintaining the bottle with the weights of 180 grams and 200 grams. Overall, the prosthesis was able to function 26 out of 30 times (87% success rate).

Table 3. Weight Effectiveness of Prosthesis

W	20 g	40 g	60 g	80 g	100 g
T1	passed	passed	passed	passed	passed
T2	passed	passed	passed	passed	passed
T3	passed	passed	passed	passed	passed

W	120 g	140 g	160 g	180 g	200 g
T1	passed	passed*	passed*	passed*	passed*
T2	passed	passed*	failed	passed*	failed
T3	passed	passed*	passed*	failed	failed

The prosthesis has fulfilled 76 trials out of 90 attempts in the whole experimental process. As the minimum requirement for it to pass as a proof of concept is 80%, the prosthesis was considered functional and effective.

4. CONCLUSION AND RECOMMENDATION

This study used various experimental tests to perform the basic functionality and show the BP prosthesis's effectiveness. It successfully functions 87% and 80% in picking and placing motions at stationary and mobile positions, respectively. As per its weighing capacity, the prosthesis was able to carry bottles in all trials for the first set; in the second set, however, it dropped the bottles with weights 160 and 200 grams. Consequently, it failed at 180 at 200 grams in the final set. Overall, it was able to pick up bottles

26 out of 30 times or at 87%. It was observed that the prosthesis had difficulty in carrying weights starting from 140 grams in all sets. All stages reached the requirement of 80% to be considered functional.

The prosthesis is functional, and the mechanical gripper with its equipped actuator has a specified degree of freedom not far from the bottles' dimensions. It is recommended that modular claw attachments with more DOF are made to execute other tasks concerning the amputee's field of work. Using an electromyogram sensor and motors to activate the prosthesis may also help reduce the user's effort upon working since the amputee uses their whole arm to execute the prosthesis's opening and closing action. It is also recommended to utilize the dominant hand for efficiency as this decreases potential PLP. Although the prosthesis's overall cost would significantly increase, a variation with the prosthesis design, most specifically with its modular adjustments, would target a larger market of possible buyers.

5. ACKNOWLEDGEMENTS

First and foremost, we would like to express our gratitude to our research supervisor, Mr. Michael Manguerra, for extending his wise knowledge to us and guiding this study with his utmost care despite his other endeavors as a university professor. He was able to instruct us with the proper way of constructing a paper, as well as pointers, to avoid writing erroneous statements that oppose the original intent of the paper. His guidance and supervision are undoubtedly appreciated. Further, we also wish to extend our heartfelt thanks to our parents, who had provided us with the materials required for this study; likewise, we are grateful for the love, patience, and support they had shown to finish the paper ultimately. Lastly, we sincerely cherish God for all His graceful blessings; all was possible because of Him.

6. REFERENCES

Berning, K., Cohick, S., Johnson, R., Miller, L. A., & Sensinger, J. W. (2014). Comparison of body-powered voluntary opening and voluntary closing prehensor for activities of daily life. *Journal of Rehabilitation Research and Development*, 51(2), 253–262. doi:10.1682/jrrd.2013.05.0123

Carey, S., Lura, D., Highsmith, J. (2015). Differences in myoelectric and body-powered upper-limb prostheses: Systematic literature review. *Volume 52*. Pages 247–262

Cooper, T. (2019). Understanding Prototype Development Phases For Medical Products. Retrieved from: <https://www.meddeviceonline.com/doc/understanding-prototype-development-phases-for-medical-products-0001>



- Guo, X., Lin, Z., Lyu, Y., Bekrater-Bodmann, R., Flor, H., & Tong, S. (2017). The Effect of Prosthesis Use on Hand Mental Rotation After Unilateral Upper-Limb Amputation. *IEEE Transactions on Neural Systems and Rehabilitation Engineering*, 25(11), 2046–2053. doi:10.1109/tnsre.2017.2702117
- Huinink, L. H., Bouwsema, H., Plettenburg, D. H., van der Sluis, C. K., & Bongers, R. M. (2016). Learning to use a body-powered prosthesis: changes in functionality and kinematics. *Journal of neuroengineering and rehabilitation*, 13(1), 90.
- Labor Code of the Philippines (2013). Handbook of Employee's Compensation and State Insurance Fund. Book IV, Title II of P.D. No. 441
- Lu, Y., Xie, Z., Wang, J., Yue, H., Wu, M., & Liu, Y. (2019) A novel design of a parallel gripper actuated by a large-stroke shape memory alloy actuator. *International Journal of Mechanical Sciences*. 159. 10.1016/j.ijmecsci.2019.05.041.
- Mina, C. (2013). Employment of Persons with Disabilities (PWDs) in the Philippines: The Case of Metro Manila and Rosario, Batangas, PIDS Discussion Paper Series, No. 2013-13
- Schweitzer, W. (2017). Technical Below the Amputee Issues- Bowden cable mount for prosthetic arm [patent, explained]. Retrieved from <https://www.swisswuff.ch/tech/?p=7172>
- Smit, G., & Plettenburg, D. H. (2010). Efficiency of voluntary closing hand and hook prostheses. *Prosthetics and orthotics international*, 34(4), 411–427. Retrieved from <https://journals.sagepub.com/doi/pdf/10.3109/03093646.2010.486390>



Comparative Analysis between the Shinyei PPD42NS and Plantower PMS7003 Low-Cost Air Quality Sensors

Camron Evan C. Ong, Kerby Matthew C. Chiu, Keziah Bryanna T. Lat,
and Mary Alaena Katelyn P. Magnaye
De La Salle University Integrated School, Manila

Hiroki Asaba and Clement Y. Ong
De La Salle University, Manila

Abstract: Particulate matter (PM) is a form of air pollution that is considered harmful as these may cause respiratory problems. PM sensors are used to measure PM in the air and vary in costs. There have been many studies done on the accuracies of these sensors based on their price. In this research, a comparative analysis was done between a low-cost sensor, the Shinyei PPD42NS, and a mid-range sensor, the Plantower PMS7003. In previous studies, there were comparisons made between low quality sensors but no direct comparison between these two sensors. The tests were done in an indoor and outdoor environment wherein sensors were placed beside each other to measure particulate matter greater than 1 micron for a continuous span of 10 hours. Results from these tests showed that the Shinyei measurements broadly follow the more expensive Plantower but have more significant deviations over short periods. Larger deviations were noted in the morning and evening periods of testing. Recommendations for further characterization are provided in this paper.

Key Words: Particulate Matter; Air Quality Monitoring; Low-cost PM sensor; Shinyei PPD42NS; Plantower PMS7003

1. INTRODUCTION

Pollution is a problem faced throughout the world and can spread to other parts of the world (National Geographic Society, 2012). Air Pollution can not only bring harm to the environment but also to the health of the population. It is the ninth leading risk factor for death, and it is responsible for 3.2 million deaths each year (Kurt et al., 2016). The statistics from the World Health Organization (WHO) in 2016 shows that 91% of the population of the world reside in places that do not meet the imposed air quality standards, and estimates that in the same year, approximately 4.2 million deaths worldwide were caused by outdoor air pollution (Ambag, 2018).

Particulate matter (PM) is a form of air pollution involving solid materials and liquid droplets. The particles may come from both natural events and man-made sources. These particles range in size and are categorized into two main groups, which are PM 10 and PM 2.5. PM 10 involves particles sized 10 micrometers and smaller, while PM 2.5 involves 2.5 micrometers and smaller. Exposure to these can pose different threats to human health and the environment both short term and long term (EPA, 2018).

Detectors are used by the government to know the quality of air. The Beta Attenuation Monitor

(BAM) is most widely used by governments and is considered the standard for detecting particulate matter in the air but is expensive to produce. While low-cost sensors are existent, they are still being developed and are still faulty and inconsistent (European Commission, n.d.). When compared to the standard particulate matter sensors, these cheap sensors are shown to be less accurate (Ahn et al., 2019). Furthermore, these sensors require specific technological components which may not be available in other places of the world.

The urgency to design and manufacture low-cost air quality sensors is widespread. Low-cost air pollution sensors enable high-quality resolutions in real-time and provide new opportunities to enhance existing sensors, as well as engage with the public in active monitoring (Castell et al., 2016). However, the quality of the data gathered is questionable. Studies have reported that low-cost sensors are unstable and often affected by atmospheric conditions (Karagulian et al., 2019).

This study aims to compare the performance between the Shinyei PPD4NS sensor and Plantower PMS7003 sensor in terms of accuracy in measuring particulate matter. Additionally, the capabilities and limitations of the Shinyei will be identified. The tests will be conducted in both an

indoor and outdoor environment, and particulate matter will be measured in concentration.

2. PM SENSORS

2.1 Shinyei PPD42NS

The Shinyei PPD42NS uses the light-scattering principle (Tan, 2013). Particulate matter present in the air is measured based on the light scattered by the particles. A heating element is present that causes air to flow in, rise through, and out of the sensor. Additionally, some guidelines are provided when using the sensor, namely that it should be vertically oriented, in a dark area, and be given time to warm up. The sensor outputs a logic low whose time is proportional to the particulate matter concentration. Results from the sensors showed that one had occasional sporadic output compared to the other (Tan, 2013).

Additionally, according to Canu et al. (2018), the Shinyei sensor gives two outputs, P1 outputs information about particles over 1 μm while P2 outputs about particles over 2.5 μm , meaning that it cannot measure certain PM sizes strictly. The sums of the duration of low outputs from P1 or P2 is proportional to the quantity of dust particles. The correlation for P1 is shown in Figure 1.

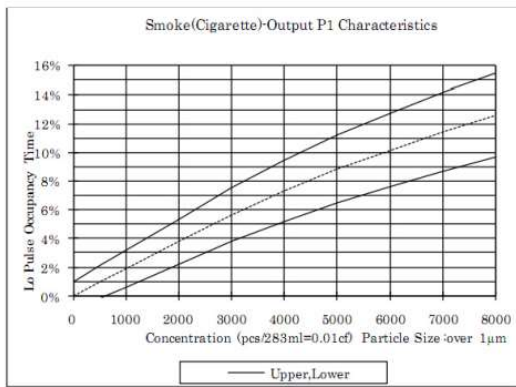


Figure 1. Relation between P1 LPO and PM concentration (Canu et al., 2018)

2.2 Plantower PMS7003

The Plantower PMS7003 uses laser scattering to measure particulate matter. The amount of light scattered due to particles are collected. The equivalent particle diameter and the number of particles with different diameter per unit is calculated by a built-in microprocessor. These measurements are provided in both $\mu\text{g}/\text{m}^3$ and in pieces per 0.1L. The Plantower is known to be effective and reliable in measuring PM (Badura et al., 2018).

3. METHODOLOGY

3.1 Data Collection Setup

Two independent systems to measure the quality of the air were developed. One is based on the Shinyei PPD42NS sensor, and the other based on the Plantower PMS7003 sensor. The Shinyei PPD42NS sensor was programmed with a code provided by SeeedStudio (2015), while the Plantower PMS7003 sensor was programmed with a code provided by Alam (2019). The sensors were set up to measure particulate matter sized greater than 1 μm and tested simultaneously in two different environments around a residence. The indoor test was conducted in a 52 m^3 room with three opened doors and only natural air flow circulating air, while the outdoor testing was done in an open-faced roofed garage.

3.2 Data Collection Method

Both sensors were set-up, connected, then interfaced through an Arduino board. As shown below in Figure 2, the Shinyei sensor was placed vertically for air to flow into the lower hole and out the upper. Additionally, data was not recorded for the first three minutes of connecting the Shinyei to allow it to first heat up its heating element which allows the flow of air in and out.

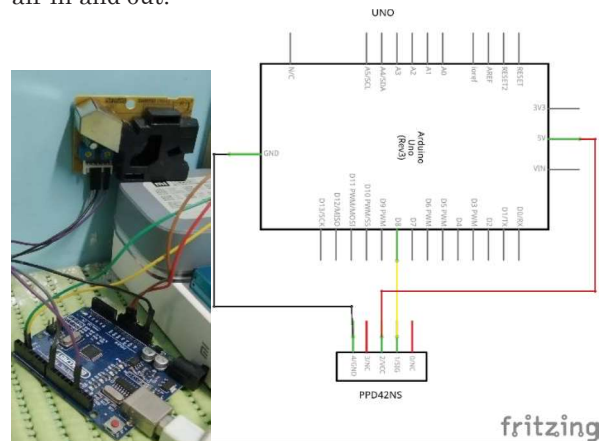


Figure 2. The setup of the Shinyei PPD42NS connected to an Arduino Board (Goram, 2019).

The Plantower was placed near the Shinyei to also obtain readings. Both sensors were interfaced through individual Arduino boards as shown below in Figure 3.

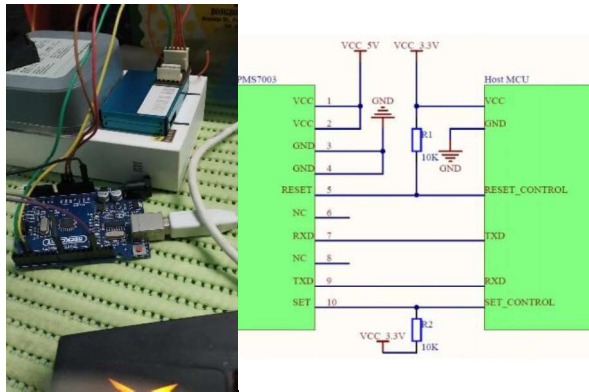


Figure 3. The Plantower PMS7003, connected to the same Arduino board (Zhou, 2016).

Data from the sensors were interfaced through the Arduino board, then transferred to Microsoft Excel to graph the readings.

3.3 Data Analysis Strategy

A conversion in the gathered data was necessary to visualize the readings of the sensors. The Shinyei PPD42NS measures in pieces per 0.01 cubic feet, while the Plantower PMS7003 measures in micrograms per liter of air. Additionally, the sensors send data at different time intervals, specifically, the Shinyei is set to send data in 30-second intervals, while the Plantower is set to 1-second intervals. After converting the data, the PM measurements were smoothed, graphed, and represented through line graphs showing the changes of the PM concentrations on the y-axis with the corresponding time on the x-axis. These graphs were used to compare and analyze the sets of data visually and statistically.

4. RESULTS

As shown below, Figure 4 shows the measurements taken from the two sensors in an indoor environment. The data collected from the Shinyei and the Plantower were done in a 10-hour test.

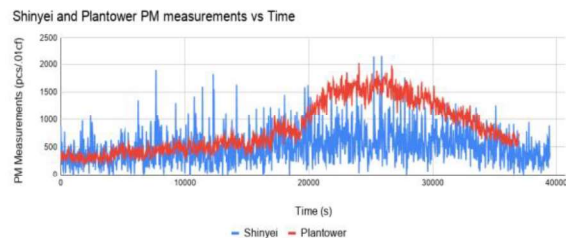


Figure 4. Original Indoor Measurements

The original data gathered is shown, represented by blue for the Shinyei, and red for the Plantower. These measurements are noisy is difficult

to be accurately analyzed, hence a smoothing function, specifically through moving average, was done. Shown below in Figure 5 are the smoothed graphs.

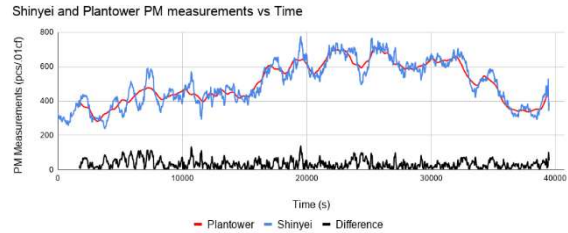


Figure 5: Smoothened Indoor Measurements

The blue line represents the Shinyei's measurements, while the red line represents the Plantower's. Both sets of data were smoothed through continuously averaging 25 data points for the Shinyei, and 15 data points for the Plantower. After time-aligning the data to match the graph, the difference between the two sensors' measurements was found, graphed and represented by the black line. It can be seen in the blue line that the Shinyei follows the trend of the Plantower's measurements throughout the test period, with a root-mean-square error (RMSE) of 41 pcs/0.01cf.

Figure 6 below shows the PM readings from the sensors in the outdoor environment. These tests were done simultaneously while each sensor was beside each other for a period of 10 hours, starting mid-morning to early evening.

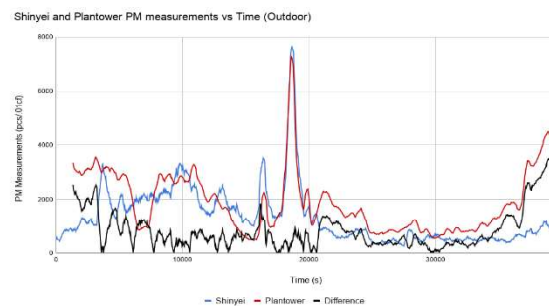


Figure 6: Smoothened Outdoor Measurements

Like the indoor graph, the blue line represents the Shinyei, and the red represents the Plantower. For this set, 15 data points were continuously averaged to attain a smoothed graph. The data was time aligned as well to attain an accurate difference measurement. The graph shows that the Shinyei had lower readings in both the earlier part of the day as well as towards the night compared to the Plantower. The middle parts of the data are similar, however. The large peaks in the middle are nearly identical, with the Shinyei having a slightly



higher reading, peaking at 7367 pcs/0.01cf whilst the Plantower peaked at 7257 pcs/0.01cf. The RMSE is 1087 pcs/0.01cf which is attributed both the differences in the morning and evening, as well as the similarities in the afternoon.

5. DISCUSSIONS

Based on the findings, the two sensors are able to produce readings which show that they can be related. This means that the Shinyei PPD42NS can match the performance of the Plantower PMS7003, but only up to a certain degree. Looking back at the time-series graphs of the indoor test, the difference of each point of data is, again, relatively small. This is a good sign as the studies of Kuula et al. (2019) found that the sensor was effective and usable as a complementary to other particulate matter sensors. However, it should be noted that even after smoothing the data, the Shinyei was still noisy in its measurements.

On the other hand, as stated previously, the Shinyei's PM measurements in the morning and evening were significantly lower compared to what the Plantower recorded. The discrepancies during these periods may indicate that temperature and relative humidity might have skewed the sensor's measurements. Jayaratne et al. (2018) and Rai et al. (2017), also believe that temperature and humidity is factor that contributes to the inconsistencies of the Shinyei sensor. Although these factors may also affect the performance of the PMS7003, it can be implied that since the Shinyei is the significantly lower costing sensor, it also has lesser tolerance to environmental influence. To add, this may have not been observed in the indoor test since walls and a roof provide significant degrees of insulation from external environmental changes.

On the other hand, Holstius et al. (2014) investigated another factor, ambient light, which could also be a factor toward the Shinyei's measurements in the morning and night. Additionally, as it was an outdoor experiment, wind may have also factored in. Since the Shinyei relies on a heating element, it relies on air density differences for its airflow. This is more easily affected by wind compared to other sensors in general, which make use of fans for consistent airflow.

That being said, the Shinyei performed well in the afternoon parts of the outdoor test wherein it followed the Plantower's graphs better than in the morning and evening. Additionally, the larger difference in the RMSE values of the outdoor test compared to the indoor is also attributed to higher PM levels outdoors than indoors.

6. CONCLUSION

The Shinyei PPD42NS is a capable low-cost air-quality sensor in terms of particulate matter measurement performance when compared with the Plantower PMS7003. The indoor test showed very promising results in accurately measuring particulate matter, whilst the outdoor test was overall decent as well despite external factors potentially affecting the Shinyei. The lower cost and bare construction allow room for modifications thus providing significant potential. Future research will investigate exposing the Shinyei to controlled PM sizes and testing its performance in more environments with controlled light levels, temperature, and relative humidity. In line with this, the study will continue to improve the Shinyei by identifying limitations and adding corrective modifications, such as fans and filters, to improve its usability and performance in measuring particulate matter.

7. REFERENCES

- Ahn, K. H., Lee, H., Lee, H. D., & Kim, S. C. (2019). Extensive evaluation and classification of low-cost dust sensors in laboratory using a newly developed test method. *Indoor Air*, 30(1), 137–146. <https://doi.org/10.1111/ina.12615>
- Alam. (2019, October 14). *Interfacing PMS5003 PM2.5 Air Quality Sensor with Arduino*. Retrieved from <https://how2electronics.com/interfacing-pms5003-air-quality-sensor-arduino/>
- Ambag, R. (2018, June 18). *How bad is air pollution in the Philippines?* Retrieved from <https://www.flipsience.ph/health/how-bad-air-pollution-philippines/>
- Badura, M., Batog, P., Drzeniecka-Osiadacz, A., & Modzel, P. (2018). Optical particulate matter sensors in PM_{2.5} measurement in atmospheric air. *E3S Web Conference*, 30, 1-8. <https://doi.org/10.1051/e3conf/20184>
- Canu, M., Galvis, B., Morales, R., Ramirez, O., & Madelin, M. (2018). Understanding the Shinyei PPD42NS low-cost dust sensor. *2018 IEEE International Conference on Environmental Engineering (EE)*. https://www.researchgate.net/publication/324171671_Understanding_the_Shinyei_PPD42NS_low-cost_dust_sensor
- Castell, N., Dauge, F., Schneider, P., Vogt, M., Lerner, U., Fishbain, B., Broday, D., & Bartonove, A. (2016, December 28). Can commercial low-cost sensor platforms contribute to air quality monitoring and exposure estimates? *Environment International*, 99, 293-302. <https://doi.org/10.1016/j.envint.2016.12.007>
- EPA. (2018, November 14). *Particulate Matter (PM) Basics*. Retrieved from <https://www.epa.gov/pm-pollution/particulate-matter-pm-basics>
- European Commission. (n.d.). *Measuring air pollution with low-cost sensors: Thoughts on the quality of data measured by sensors*. Retrieved from <https://ec.europa.eu/environment/air/pdf/Brochure%20low-cost%20sensors.pdf>
- Goram, M. (2019, March 31). *What Is the Air Like?* Retrieved from <https://www.hackster.io/baqwas/what-is-the-air-like-a47d8a>



- Holstius, D. M., Pillarisetti, A., Smith, K. R., & Seto, E. (2014, January 27). Field calibrations of a low-cost aerosol sensor at a regulatory monitoring site in California. *Atmospheric Measurement Techniques Discussions*, 7, 605-632. <https://doi.org/10.5194/amt-7-1121-2014>
- Jayarathne, R., Liu, X., Phong, T., Dunbabin, M., & Morawska, L. (2018). The influence of humidity on the performance of a low-cost air particle mass sensor and the effect of atmospheric fog. *Atmospheric Measurement Techniques*, 11, 4883-4890. <https://doi.org/10.5194/amt-11-4883-2018>
- Karagulian F., Barbieri, M., Kotsev, A., Spinelle, L., Gerboles, M., Lagler, F., Redon, N., Crunaire, S., & Borowiak, A. (2019, October 3). Review of performance of Low-cost Sensors for Air Quality Monitoring. *Atmosphere*, 10(9), 506. <https://doi.org/10.3390/atmos10090506>
- Kuula, J., Kuuluvainen, H., Ronkko, T., Niemi, J. K., Saukko, E., Portin, H., ... Timonen, H. (2019). Applicability of Optical and Diffusion Charging-Based Particulate Matter Sensors to Urban Air Quality Measurements. *Aerosol and Air Quality Research*, 19, 1024-1039. doi: 10.4209/aaqr.2018.04.0143
- National Geographic Society. (2012, October 9). *Pollution*. Retrieved from <https://www.nationalgeographic.org/encyclopedia/pollution/>
- Rai, A. C., Kumar, P., Pilla, F., Skouloudis, A. N., Sabatino, S. D., Ratti, C., Yasar, A., & Rickerby, D. (2017, June 29). End-user perspective of low-cost sensors for outdoor air pollution monitoring. *Science of the Total Environment*, 607-608, 691-705. <https://doi.org/10.1016/j.scitotenv.2017.06.266>
- SeeedStudio. (2015, September 23). *Grove-Dust Sensor User Manual*. Retrieved from https://www.mouser.com/datasheet/2/744/Seeed_101020012-1217636.pdf
- Tan D. (2013, July 24). *Testing the Shinyei PPD42NS*. Retrieved from <http://irq5.io/2013/07/24/testing-the-shinyei-ppd42ns/>
- Zhou, Y. (2016). Digital universal particle concentration sensor (2.5). [Datasheet]. Retrieved from https://download.kamami.com/p564008-p564008PMS7003%20series%20data%20manua_English_V2.5.pdf



FoFi: The Development of a Handheld Monitoring Device in Predicting Naturally Occurring Forest Fires

Riley Esybel O. Baguinon, Marielle C. Batinga, Joaquin Antonio L. Dayrit
and Mon Nicolai T. Estrella

De La Salle University Integrated School, Biñan City, Laguna

Abstract: Forest fires, which are natural or artificial burning of woodlands, negatively affect people and the environment. In the Philippines, Cordillera is one of the hotspots for forest fires, with approximately 122 forest fire incidents. Thus, developing a monitoring device for the early prevention of forest fires would reduce these incidents' frequency. This research aimed to create a handheld prototype device, FoFi, that gathers quantitative data which can be used with the Department of Natural Resources's data science and predictive analytics. Using an Arduino Microcontroller and sensors, the device will collect and send data. Two phases were conducted to create a monitoring prototype device for predicting forest fires. According to the results, the temperature and humidity (DHT-22) sensor showed reliable data since it can detect temperature under normal conditions, having a mean of 30.65°C; also, it precisely recorded the relative humidity with a mean of 7.89%. The Global Positioning System (GPS) module obtained a mean error of 7.251 m, which exhibited accuracy in detecting GPS coordinates. Additionally, the Globe SIM showed efficiency for Global Systems for Mobile (GSM) communication since the mean length of time for sending a message is 5.022 s. On the other hand, the gas sensor (MQ-2) and photoresistor lacks sensitivity when used; thus, a more sensitive sensor is recommended. In conclusion, the handheld device was able to achieve its purpose of monitoring forest fires.

Key Words: forest fires; handheld monitoring device; arduino microcontroller

1. INTRODUCTION

A forest fire is the burning of temperate woodland due to natural or human causes (United Nations, n.d.), which can turn uncontrollable due to environmental factors such as wind or topography. The effects of forest fires include the degradation of fauna and flora, increased carbon dioxide levels, and a compromised natural cycle. The increased carbon dioxide levels also contribute to climate change and soil erosion (Perez, 2017). Particulate matter combined with toxic gases such as carbon monoxide (CO) can cause health problems such as heart disease (Stefanidou et al., 2008). The economy has also been negatively affected by forest fires. This is because the costs to recover from these incidents have exponentially risen. In 2015, Indonesia's cost to suppress forest fires amounted to 14 billion dollars (Hirschberger, 2016) and approximately 63 billion dollars for the United States (Thomas et al., 2017).

Furthermore, the Forest Management Bureau (FMB) Chief under Forest Protection stated that the FMB and the DENR imposed a protection system called 'LAWIN,' which uses open-source technology to provide geospatial data analysis obtained from forests. It provides a data model for

identifying forest conditions, including information on practical solutions in response to the data imparted.

Dumlao (2019) reported that from January to March 2019, the Bureau of Fire Prevention in Cordillera reported 90 occurrences of the forest fire that have damaged at least 140,000 hectares of forest in Cordillera alone. Agoot (2019) indicated that Cordillera had approximately 122 forest fire incidents. These incidents implicate Cordillera as a hotspot for forest fires.

In this study, the researchers designed and developed a multi-sensor monitoring device called FoFi (from *forest fires*). It aimed to gather data to aid data science researchers for better prediction of naturally occurring forest fires.

Since studies showed that forest fire incidents had increased annually, immediate prevention is essential. Proper wildfire management is about effective communication of information regarding forest fires and technological advancements aid in optimizing effective forest fire detection systems (Molina-Pico et al., 2016). With this, FoFi, from the word forest fires, will help in monitoring forests. The contribution of LAWIN to forestry is significant; however, it only focuses on managing forests to avoid

deforestation and degradation, whereas FoFi aims to collect data to predict forest fires.

This study's findings will benefit society and the academic community since it tackles how citizens can protect the forest environment and avoid such disasters. Also, government agencies such as DENR and FMB may benefit from this because this can aid in gathering quantitative data about the status of forests. The increase of forest fires in the Philippines means that this should be addressed immediately so that society members can face such calamities better or even prevent.

2. METHODOLOGY

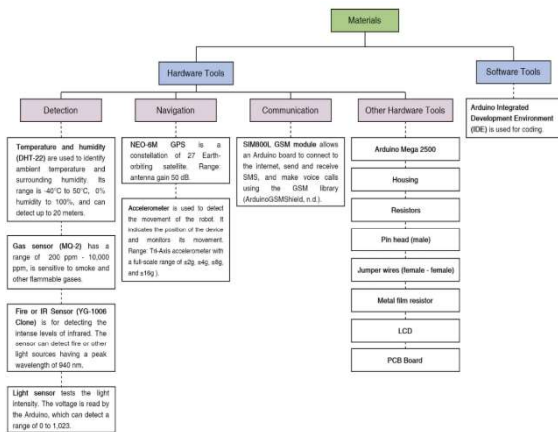


Fig. 1. List of materials needed for the handheld device.

The list of requirements, together with the knowledge gathered about the various devices and sensors, was used to plot out the materials needed for FoFi. Arduino was strictly used for the microcontroller and programming language to create a monitoring system for forest fires. The components used were interfaced together and a GSM module was used as there are cell towers present in the targeted forest areas. Moreover, this research was conducted using a fire and environment simulation and not in an actual forest environment. The intent of this was to test the efficiency of the device in gathering data and not its durability. The sensors were limited to what was listed in Figure 1. Additionally, there were two phases in conducting the study: evaluating the sensors and refining FoFi.

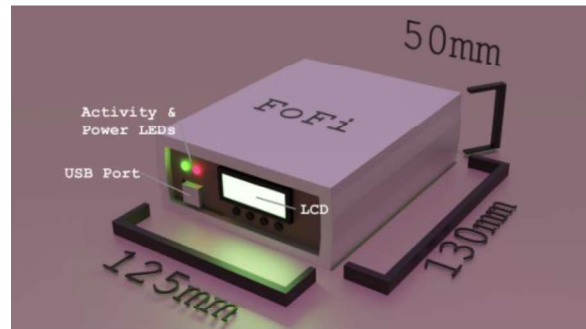


Fig. 2. A 3D draft model of FoFi.

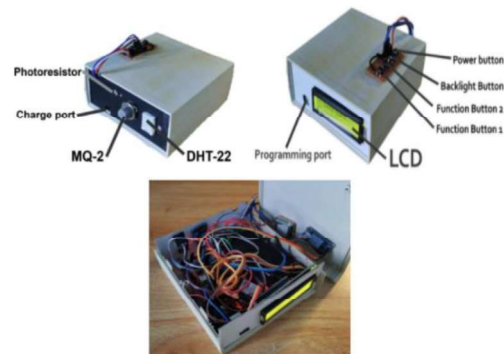


Fig. 3. Final version of FoFi with sensors pieced together.

With a general idea of the housing and hardware, a draft 3D model was made using Blender 2.9. there were some changes in piecing all the components together for the final device. Figure 3 shows the final version of FoFi. Unlike the draft, the buttons were moved on top due to the lack of space caused by the LCD driver board. The rest remain the same with the LCD and USB port being in front while the sensors and charging port are at the back.

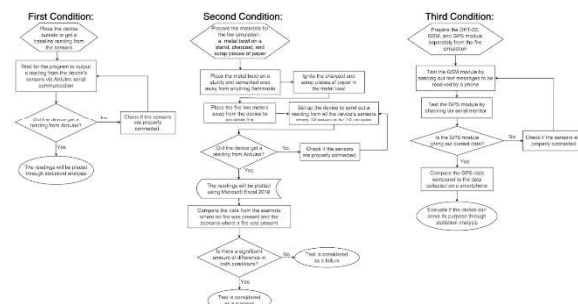


Fig. 4. Evaluation of the handheld device.

According to Figure 4, there were three conditions in evaluating FoFi. In the first condition, the sensors were tested on a normal setting, without fire. The device was then tested in a fire simulation for the second condition. For the third condition, some



sensors were tested separately from the fire simulation. The conditions were evaluated using statistical analysis to gather quantitative data. Also, it involved the estimation of parameters to gauge the mean parameters of the data collected and hypothesis testing, which determined the reliability of the data. A quantitative experimental research design was used to test the ability of each sensor to collect data.

The prototype was refined to ensure that the device can successfully gather data. This involved fixing the device to resolve any issues that were identified during the testing phase. There were four challenges encountered during building FoFi. First, the MQ-2 and IR sensors were not functioning correctly. Both sensors were then retested at different conditions to double-check their functionality. Second, there was a defect in the ability of the GPS module to provide data. However, after re-examining it, the sensor only needs a few minutes to lock onto satellites before providing the data. Also, reprogramming the Arduino enabled detection regarding whether the GPS module is ready. Third, there was an issue with the Arduino Mega's serial communication. After thorough testing, it was determined that the TX and RX pins were interchanged and the GSM module only works on Serial IO 1 and not on other serial ports due to its need for serial interrupts. Lastly, insufficient current was evident while testing; the Arduino and sensors were not able to run through USB power from a laptop; thus, the rechargeable battery was used during the testing.

3. RESULTS AND DISCUSSION

Statistical analyses were interpreted using Microsoft Excel 2019. The estimation of the true mean parameters of primary data is determined at a 5% level of significance. A two-tailed test at a 5% level of significance tested the null hypothesis of whether the mean parameters of primary data are significantly comparable to the mean parameters of data obtained from the data collection stage or other studies.

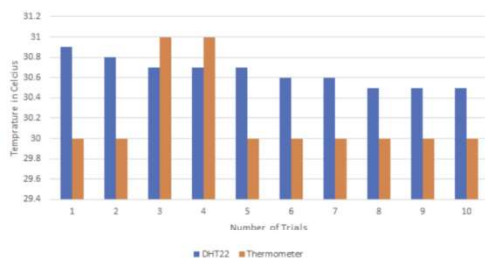


Fig. 5. Temperatures recorded by the DHT-22 sensor and thermometer.

Table 1. Data analysis for ambient temperature recorded using DHT-22 sensor.

Mean (°C)	30.65
Standard Deviation	0.1285
Variance	0.0165
Estimation of Parameters (One Population Mean) ² at $\alpha = 5\%$	30.65 ± 0.0796
Hypothesis Testing (One Population Mean) ² at $\alpha = 5\%$, t-test	Ho: $\mu = 30.20$; Ha: $\mu > 30.20$ p-value: 1.0000, $t > 1.8331$ or $p > 0.05$, reject Ho.

1 - recorded on 1/18/21 from 4:06 to 4:30 pm; mean temperature noted with thermometer (°): 30.20°C

A DHT-22 sensor is used to detect temperature and humidity. Its range is -40°C to 50°C, 0% to 100% humidity, and it can detect up to 20 meters. Given the mean temperature recorded

(°) by the thermometer, there is proof that the sensor is accurately detecting temperatures in normal conditions. Though Trials 3 and 4 were the only trials wherein the sensor detected lower temperatures than the thermometer, the difference is not significant enough to warrant misinterpretation. However, Obanda (2017) did not compare the sensor readings with a thermometer to test accuracy; the grove temperature sensor used successfully detected temperature changes. Similarly, the DHT-22 was more precise as it had an accuracy of ±0.5°C compared to the grove sensor's which was ±1.5°C. Although the grove sensor can read up to 125°C compared to 80°C from the DHT-22, the device is not aimed to detect extreme temperatures.

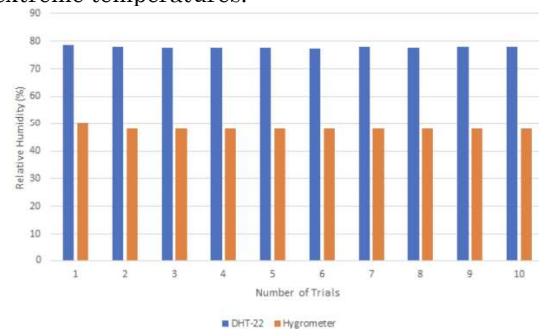


Fig. 6. The data from the DHT-22 sensor when tasked to read the relative humidity.

Table 2. Data analysis for relative humidity using a DHT-22 sensor.

Mean (%)	77.89
Standard Deviation	0.3562
Variance	0.1269
Estimation of Parameters (One Population Mean) ² at $\alpha = 5\%$	77.89 ± 0.2208
Hypothesis Testing (One Population Mean) ² at $\alpha = 5\%$, t-test	Ho: $\mu = 48.20$; Ha: $\mu > 48.20$ p-value: 1.0000, $t > 1.8331$ or $p > 0.05$, reject Ho.

2 - Data recorded on 1/18/21 from 4:06 to 4:30 pm; mean temperature noted with thermometer during this period (°): 48.20%

Given the mean relative humidity recorded (°) by the thermometer, there is proof that the sensor recorded relative humidities but inaccurately. The sensor's mean humidity records are significantly higher than the humidity recorded by the thermometer, which may lead to misinterpretation of data. The sensor's data was precise, indicating that further tests can be conducted to compensate for the unusually high readings with software.

The MQ-2 sensor is sensitive to smoke and has a built-in potentiometer to adjust its sensitivity for digital output (Mukherjee, 2016). Across ten trials, only the first trial showed a value of 2 parts per million (ppm) for CO and 0 ppm for the other trials. In detecting LPG, it reported 0 ppm across all trials as no LPG was present during the testing. This was included in the testing to determine a possibility of a trend in LPG readings. Like the CO tests, the first test showed 2 ppm for a smoke while the rest showed 0 ppm. This is similar to Niranjana and HemaLatha's (2018) findings, as they found that the range of raw data given was 45 to 80 ppm without smoke and 100 to 250 ppm with smoke. Conclusively, the sensor did not detect smoke, LPG, or carbon monoxide levels accurately enough to be used in the device.



Fig. 7. The YG-1006 sensor's data regarding the detection of infrared levels

The infrared sensor (YG-1006) can detect fire or other light sources having a peak wavelength of 940 nm. According to Figure 7, in the trial without fire, all ten trials reported a fire which are attributed to the presence of sunlight during testing. When placed 0.10 meters away, all ten trials also reported fire. Furthermore, when placed 0.15 meters away, 30% of the trials detected fire, and when placed 0.20 meters away, half of the trials detected fire. This indicates that a YG-1006 sensor would be impractical as it may detect sunlight as infrared. Although Obanda (2017) recommended to use a YG-1006 sensor instead of a light sensor, the results still reported inconsistencies due to the presence of sunlight.

The light sensor (photoresistor) can be used together with a 10k ohm resistor connected to the ground to give various voltage outputs. This is then read by the Arduino's analog input which could provide a range of values from 0 to 1023. The device was subject to three scenarios (10 trials per scenario):

- A scenario with no light

- A scenario where a light source is placed 5cm away
- A scenario with the light source directly on the sensor

The values obtained from this sensor were consistent across all 10 trials for all 3 scenarios; however, due to the sensor only giving various voltages and depending on the analog read pins of the Arduino, the values do not have any standardized unit of measurement such as lux. This is a problem as it could lead to inconsistencies across multiple devices and potentially negatively affect the effectiveness of data science research.

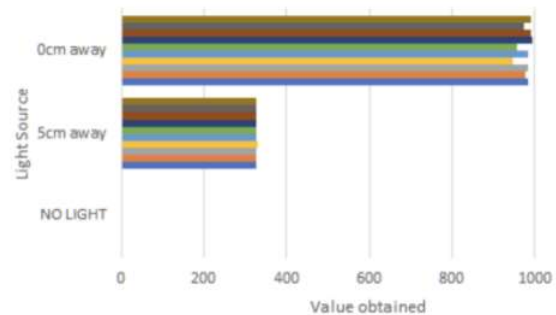


Fig. 8. The photoresistor's data in varying lighting conditions

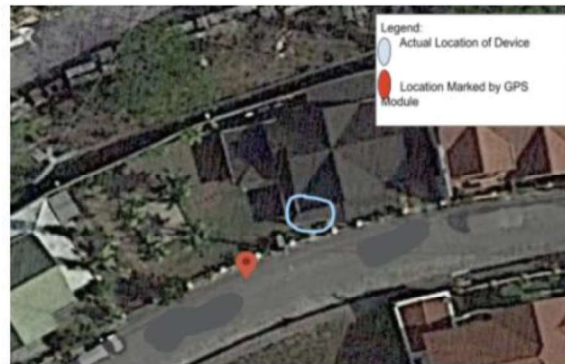


Fig. 9. The GPS module's data regarding the GPS coordinates on Trial 1

Furthermore, the GPS is a navigation system that has a range of antenna gain 50 dB. By obtaining the coordinates and inputting it in Google Maps, the GPS data, highlighted by the red pin is seen to be relatively close to the actual location of the device.



Table 3. Data analysis for GPS module

Accuracy of GPS Module in Documenting Coordinates	
Mean	7.2510
Standard Deviation	4.5876
Variance	21.046
Estimation of Parameters (One Population Mean) ² at $\alpha = 5\%$	7.2510 ± 2.8434
Hypothesis Testing (One Population Mean) ² at $\alpha = 5\%$, t-test	Ho: $\mu = 12.5$; Ha: $\mu < 12.5$ p-value: 0.0001, $t < 1.8331$ or $p < 0.05$, reject Ho.

3 - Reference parameters of error readings of GPS coordinates obtained from Islam and Kim (2014); $\mu: 12.5$ m

Table 3 shows that the GPS module accurately identified the GPS coordinates, with a mean error reading of 7.251 meters from the device's actual location. The mean error distance of the GPS readings is also significantly lower than the error readings obtained by Islam and Kim (2014). Conclusively, the GPS module is more accurate and precise in recording data.

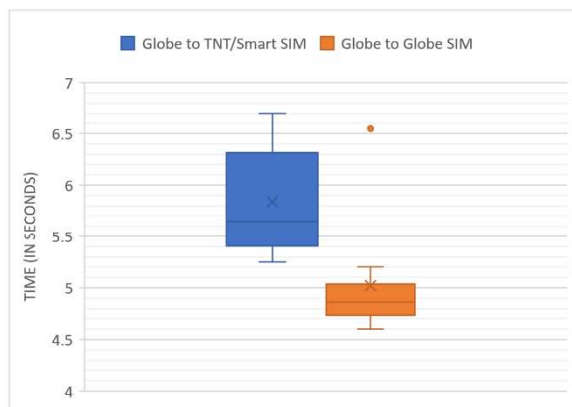


Fig. 9. The data of the GSM regarding communication through text messaging.

Table 4. Data analysis for GSM text messaging.

Length of time for messaging to be sent using GSM Module	SMART/TNT SIM	GLOBE SIM
Mean (s)	5.842	5.022
Standard Deviation	0.4988	0.5330
Variance	0.2488	0.2841
Estimation of Parameters (Difference of Two Population Means) at $\alpha = 5\%$	0.8200 ± 0.4525	
Hypothesis Testing (Difference of Two Population Means) at $\alpha = 5\%$, t-test	Ho: Smart = Globe Ha: Smart > Globe p-value: 0.9998, $t > 1.645$ or $p > 0.05$, reject Ho.	

Meanwhile, the GSM module allows the Arduino board to send and receive SMS and make voice calls using the GSM library. The mean length of time for sending a message to TNT or Smart SIM is 5.842 s, while Globe SIM is 5.022 s. The time difference between the SIMs is significant since the device must send out information quickly. Thus, the Globe SIM is more efficient for GSM text messaging. Moreover, Mr. Nahial stated that cell towers are available in Cordillera since it is used by the people living near the forest. Obanda (2017), who used a SIM900 module, found that text messages took as little as 45 seconds and as long as 80 seconds, which is longer than FoFi's data. However, this could be due to the different carriers they used and other factors.

4. CONCLUSIONS

Forest fires are natural disasters that endanger natural and human resources. In the Cordillera region in the Philippines, data science is being used to predict the subsequent forest fires, prompting the researchers to create a handheld device that forest rangers can use to gather quantitative data to support the LAWIN system's qualitative data.

Readily available electronic components were interfaced with the Arduino microcontroller and were tested to gauge their performance in the context of forest monitoring. The results showed that the YG-1006 IR sensor is too inconsistent to be used in recreating a similar device. The MQ-2 sensor and photoresistor should be replaced with more capable alternatives. On the other hand, the DHT-22 accurately gathered data for ambient temperature. However, it would require tuning for reading relative humidity. Also, the GPS and GSM modules were effective in identifying coordinates and sending information. Overall, FoFi can significantly contribute to the prediction of forest fires.

5. ACKNOWLEDGMENTS

The researchers would like to express their gratitude to the De La Salle University for the research fund; their research mentors, Miss Sherilyn Abarra, Miss Leah Madrazo, and Dr. Kerry Cabral; their research adviser, Miss Myrlla Torres; and their former robotics teacher, Sir Morris Bana. The researchers would also like to thank the former researcher of DENR, Mr. Sherwin Nahial, together with the FMB Chief under Forest Protection, for helping with the gathering of information regarding forests and forest fire. Lastly, the researchers would like to acknowledge their families and friends for their support while the research was in progress. This research would not have been possible without these people.



6. REFERENCES

- Agoot, L. (2019, March 12). Cordillera records 165 fires in less than 3 months. Philippine News Agency. Retrieved from <https://www.pna.gov.ph/articles/1064363>
- Dumlao, A. (2019, March 8). BFP: 140k hectares of forest in Cordillera damaged in fires since January. Philstar. Retrieved from <https://www.philstar.com/nation/2019/03/08/1899759/bfp-140k-hectares-forest-cordillera-damaged-fires-january>
- Hirschberger, P. (2016). Forests ablaze: Causes and effects of global forest fires. WWF Deutschland. Retrieved from <https://mobil.wwf.de/fileadmin/fm-wwf/Publicationen-PDF/WWF-Study-Forests-Ablaze.pdf>
- Islam, M., & Kim, J. M. (2014). An effective approach to improving low-cost GPS positioning accuracy in real-time navigation. *The Scientific World Journal*, 2014, 1-8. <https://doi.org/10.1155/2014/671494>
- Molina-Pico, A., Cuesta-Frau, D., Araujo, A., Alejandre, J., & Rozas, A. (2016). Forest monitoring and wildland early fire detection by a hierarchical wireless sensor network. *Journal of Sensors*, 2016. <https://doi.org/10.1155/2016/8325845>
- Mukherjee, A. (2016). Smoke detection using mq-2 gas sensor. Retrieved from <https://create.arduino.cc/projecthub/Aritro/smoke-detection-using-mq-2-gas-sensor-79c54a>
- Niranjana, R., & HemaLatha, T. (2018). An autonomous iot infrastructure for forest fire detection and alerting system. *International Journal of Pure and Applied Mathematics*, 119(12), 16295-16302. Retrieved from <https://acadpubl.eu/hub/2018-119-12/articles/6/1512.pdf>
- Obanda, Z. (2017). Multi-sensor fire detection system using an arduino uno microcontroller (Doctoral dissertation, Strathmore University). Retrieved from <https://suplus.strathmore.edu/handle/11071/5686>
- Perez, J. (2017). Causes et consequences of forest fires. Retrieved from <https://www.ompe.org/en/causes-et-consequences-of-forest-fires/>
- Stefanidou, M., Athanaselis, S., & Spiliopoulou, C. (2008). Health impacts of fire smoke inhalation. *Inhalation Toxicology*, 20(8), 761-766. <https://doi.org/10.1080/08958370801975311>
- Thomas, D., Butry, D., Gilbert, S., Webb, D., & Fung, J. (2017). The costs and losses of wildfires. Special Publication NIST SP-1215. <https://doi.org/10.6028/NIST.SP.1215>
- United Nations. (n.d.). Forest Fire. Retrieved from <http://www.un-spider.org/disaster-type/forest-fire>



Electronic Cartero Machine (ECM): An RFID-Based One-Way SMS-Sending Kiosk

Carla Allyxzandra C. Biag
Tarlac Montessori School, Tarlac City, Tarlac

Abstract: The study's goal was to see whether a one-way text messaging machine using RFID will be effective to the students, teachers, and parents/guardians. The study has taken advantage of the school's usage of RFID to record the attendance. The same RFIDs are to be used to register into the Electronic Cartero Machine (ECM). The researchers built a system where students can message their parents/guardians their concerns by tapping the students registered RFID using the Raspberry Pi as a controller to show the GUI (Graphical User Interface) of the system. The main program is custom made using Java SE (Standard Edition) and Swing. There are 20 respondents to the survey, consisting of the students, teachers, parents/guardians, and administrative staffs to evaluate the appearance, maintainability, ease in usage and accuracy. The survey uses general acceptability indicators to describe the mean of the outcome. From the results of the survey, the appearance mean is 4.25 which suggests that the design of the ECM, especially the GUI is clear and identifiable, the maintainability mean is 4.7 which indicates that it can easily be maintained. Ease in usage is 4.9 which means that it can send the text messages to the proper recipients. The overall mean is 4.5675. It scored "Excellent" on the general acceptability indicators. Furthermore, the researchers discovered that the ECM is similar with the regular cellular phones in terms of sending time. Also, the number of characters being sent affects the sending time of the ECM.

Key Words: SMS; RFID; GUI; no cellular phone policy; communication

1. INTRODUCTION

RFID stands for Radio Frequency Identification which is an auto recognition technology that allows RFID reader to read data from RFID tags (labels) via wireless communication or better to say via radio signals from a distance (Scanlan, 2015).

The principle of using RFID to track things is used by many schools today to keep track of the students' attendance, students' time of arrival and departure from school that then texted to the students' parents.

The Lyceum of the Philippines University creates a Laguna Student Electronic Attendance and Logging System. This study was developed to create an electronic attendance and logging system using Radio Frequency Identification (RFID) and Short Messaging Service (SMS) with a web-based management system portal that allows user to access real time data to ensure campus security and smart information management.

Currently, with the widespread use of technology, the Department of Education (DepEd) in the Philippines has issued Department Order (DO) No. 83, s. 2003 - Reiteration to DECS Orders Nos. 70, s. 1999 and 26, s. 2000 - Prohibiting Students of Elementary and Secondary Schools from Using Cellular Phones and Pagers During Class Hours.

With order being implemented, students are not allowed to bring cell phones, an example of a school implementing such policy is the school of the researcher.

In this line, the researcher is making a proactive approach that can help improve communication between students and parents in case a message is needed to convey in any given situation. Using this system, just tap their RFID, screen will be activated, type your message, press send and will automatically send the text message to any GSM network of parent's registered number, then will prompt the message has been sent and will log out automatically to serve the next student.

1.1 Statement of the Problem

The study aims to provide a more efficient system of communication between the students of Tarlac Montessori School and their attending guardians.

The study also aims to answer the following questions:

1. How can the Electronic Cartero Machine be described in terms of:
 1. Appearance;
 2. Maintenance;
 3. Ease in usage ;



4. Accuracy?
2. Is there a significant difference between the ECM and the regular cellular phone in terms of sending time?
3. Is there a significant relationship between the sending time of the ECM and the number of characters sent?
4. What are the implications of the ElectronicCartero machine to the society?

1.2 Significance of the Study

The purpose of this study is to strengthen the communication between the attending guardians and students during the students' time in school. With this study, the school would have an alternative communication system which can be utilized when a student needed to message their parents because of an emergency or because they needed something.

This study will significantly benefit the attending guardians students, and the school administrations.

1.3 Scope

The researchers' proposed system will be using the idea or concept of the current system of the RFID of Tarlac Montessori School (which notifies parents/guardians if their child has entered or left the school campus) and enhance it by adding an SMS so that the student will be able to send a message to the parents/guardians regarding specific topics using their own RFIDs. The system can be used by all schools that have acquired or will acquire for an RFID system.

2. METHODOLOGY

2.1 Experimental Design

The researchers developed an RFID-Raspberry Pi-GSM System to test the one-way text processing system that will be needed in the study. Figure 1 shows the System Block Diagram. The main program is custom made using Java SE (Standard Edition) and Swing [GUI (Graphical User Interface) Development Language for Java] or simply Java program. For an RFID and GSM system to link to Java program, the programmers use AT (Attention), expect and bash (Bourne Again Shell) programming languages. As shown in the Figure 1, the student's ID is used to tap the ID to RFID reader. The RFID reader will forward the information to the data base on Raspberry Pi. The RFID information embedded will served as login authentication to enter the system. The ID should be registered to the system, otherwise a message will prompt that the student is not a registered user and cannot use the system until the student completed the registration process.

System Administrator is responsible to process the addition of user/s in the system. Once the system recognized that the student is a valid user, a GUI (Graphical User Interface) will appear to the LCD monitor processed using Raspberry Pi running on Raspbian OS (Operating System). Java JRE (Java Runtime Environment) is also installed in the Raspbian to run the Java program. The student can send the SMS message to his/her parent's cell phone numbers regardless of their carrier's network. The system is capable to identify and process SMS in any network. The GSM System is used to process any SMS to and from the Raspberry Pi. The sender or student can see two previous successful message sent by the parent or guardian found in Inbox as shown in Figure 4.

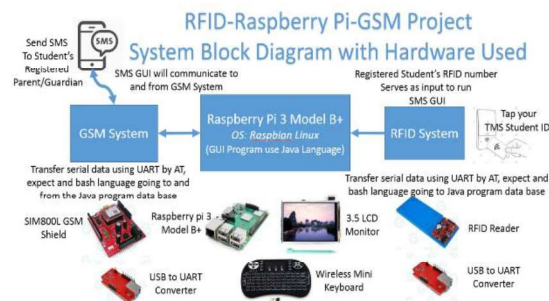


Figure 2. RFID-Raspberry Pi-GSM Project System Block Diagram

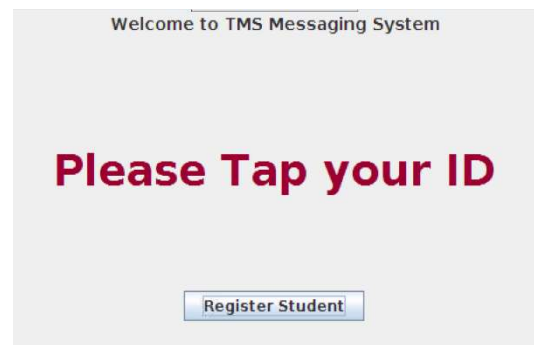


Figure 3. Main GUI Design

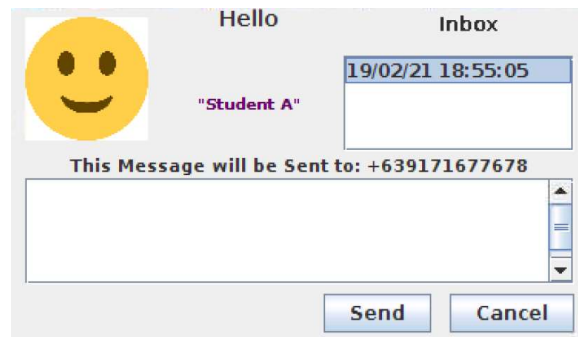


Figure 4. SMS GUI Design

Please click the 'Scan' button and Badge your ID to Activate this Form

*RFID Number:

*Student Full Name:

Student Photo Location:

*Guardian Full Name:

*Guardian Mobile Number:

Figure 5 shows the Registration GUI Design

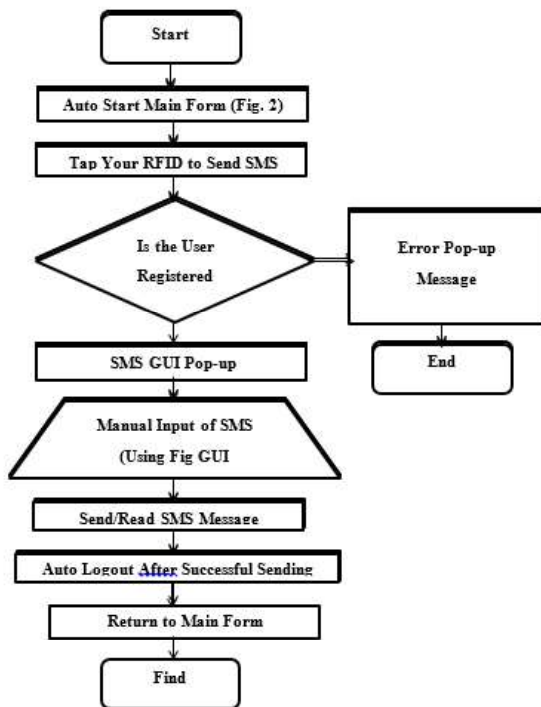


Figure 6. The Flowchart if Sending SMS

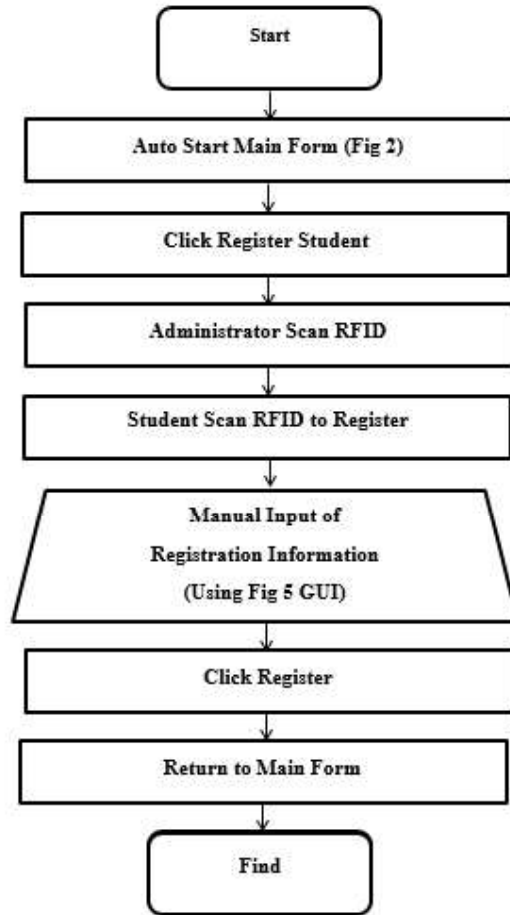


Figure 7. The Flowchart of Registration

The system was be tested by random students, teachers, parents/guardian, and administrative staffs using the effectiveness, reliability, and maintainability criteria.

To assure the quality of the RFID-Raspberry Pi-GSM System, the researchers asked the help of the school's System Engineer and Programmer to check and evaluate on the system functionality and make sure that it will be able to send the one-way text message to the parents of the students at any cases and everything is considered. This will fault proof and be able to correct the bug/s in case it will be found out. Aside from technical checking, the researchers also asked the Systems Engineers to evaluate the system in terms of effectiveness, reliability, and maintainability.



2.2 Experimental Procedures

- A. Assembly and Preparation of Raspberry Pi System and Peripherals
- B. Testing the hardware and system function
- C. Program Design and Programming
- D. Testing, Evaluation, and Prototyping
- E. Respondents' Testing and Evaluation

2.3 Data Gathering Instruments

After the respondents tested the device, the researchers gave them a questionnaire that will rate the device based on the three criteria: effectiveness, reliability, and maintainability. The data that the researchers gathered were used in helping to address the problems that is sought to be answered by the study.

2.4 Statistical Treatment

Statistical Tools were used to measure the appearance, maintainability, ease in usage and accuracy was mean on the one-way text messaging system or RFID-Raspberry Pi-GSM System. The Two Sample T-Test assuming equal variance and the Pearson Product Moment Coefficient of Correlation were used to determine the significant difference and relationships in the study.

Pearson's r

$$r = \frac{nxy - (x)(y)}{n^2 - (x)^2 - (y)^2}$$

T-Test

$$t = \frac{1 - 2d_0 \sqrt{1/n_1 + 1/n_2}}$$

2.5 Indicators

Table 1
General Acceptability Indicator

Integral Value	Interval	Description
1	1.00 – 1.80	Poor
2	1.81 – 2.60	Fair
3	2.61 – 3.40	Good
4	3.41 – 4.20	Very Good
5	4.21 - 5.00	Excellent

Table 1 shows the integral value with the corresponding description of the general acceptability indicator.

3. RESULTS & DISCUSSIONS

These are the findings from the tests conducted in this study and the interpretation of these findings.

Table 2
Average scores of the One-way text messaging system using RFID

Respondents	Mean score per indicator:			
	Appearance	Maintainability	Ease in Usage	Accuracy
High School Teachers	4	5	4.5	5
Grade School Teachers	4.5	4.5	5	5
Pre School Teachers	5	5	5	5
High School Parents	5	4.5	5	5
Grade school parents	3.5	4.5	4.5	4.5
Preschool Parents	3	5	4	5
IT Specialists	4.5	5	5	5
Office Staffs	4.5	4.5	5	4.5
Yayas	4	4.5	5	5
Students	4.5	4.5	5	5
General Average	4.25	4.7	4.8	4.9

Table 2 shows the average score the One-way text messaging system using RFID acquired in terms of appearance, maintainability, ease in usage and accuracy in the survey that was conducted to the following people; two (2) High school teachers, two (2) Grade school teachers, two (2) Preschool teachers, two (2) High school parents, two (2) Grade school parents, two (2) Preschool parents, two (2) IT specialists, two (2) Office staff, two (2) yayas, and two (2) students. Table 2 also shows the general average the One-way text messaging system acquired in terms of the five (5) aspects mentioned.



Table 3
General Description for the One-way text messaging system using RFID

General Acceptability Indicators	Mean Score per indicator	Description per indicator	General Mean	General Description
Appearance	4.25	Excellent	4.5675	Excellent
Maintainability	4.7	Excellent		
Ease in Usage	4.8	Excellent		
Accuracy	4.9	Excellent		

As the table shows, the mean scores the One-way text messaging system using RFID acquired in terms of appearance is 4.25 which translates to excellent in the description indicator. This suggests that the design of the One-way text messaging system, especially the GUI is clear and can be identified easily.

In terms of Maintainability, the One-way text messaging system using RFID garnered a mean of 4.7 which is considered as excellent. This indicates that it can easily be maintained by the people in charge of it and that it is not too costly to operate.

The One-way text-messaging system using RFID, in terms of Ease in Usage, garnered a mean score of 4.8 which is equivalent STET. This means that the One-way text messaging system is easy to understand and operate or that it is user-friendly in general.

With a 4.9 mean score, the One-way text messaging system using RFID is very good in terms of accuracy. This means that the One-way text messaging system is capable of and is good in sending the text messages to the proper recipients. Also, this means that the system can record the correct data (phone number, of students) for each RFID.

Overall, the general mean the One-way text messaging system using RFID acquired is 4.5675 which is considered to be very good. This means that the one-way text-messaging system is acceptable and has received a high score in terms of appearance, maintainability, ease in usage and accuracy.

Table 4
Difference on the Sending Time of the ECM and Cellular Phone

Variables	Means	α Level	df	Critical Value	t-Stat	Decision
ECM	7.09	0.05	8	2.3060	0.4879	Do not Reject Ho
Cellular Phones	7.51					

Table 4 shows the difference on the sending time of the ECM and of regular phones. It can be seen that at alpha level 0.05, degree of freedom of 8, the critical value is 2.3060; comparing this to the computed t-statistic of 0.4879, the null hypothesis is not rejected. Thus, there is no significant difference on

the sending time of the ECM and of regular phones. It can also be inferred that the ECM and the regular cellular phones have the same sending time. Thus, in terms of time in sending, the two resources are just the same.

Table 5
Relationship Between the Number of Characters and Sending Time of the ECM

Variables	Means	α Level	df	Critical Value	r-Stat	Decision
Characters	30	0.05	7	0.666	0.7822	Significant
Sending Time	8.19					

Table 5 shows the relationship between the number of characters sent and the time required to send these by the ECM. It can be seen that at 0.05 level of significance and critical value 0.666 the computed r-stat, 0.7822 will reject the null hypothesis. Thus, there is a significant relationship between the sending time of the ECM and the number of characters sent. This infers that the number of characters being sent by the ECM will affect the sending time of the ECM.

4. CONCLUSION

One of the alternative solution to send SMS inside the school campus from a TMS student to parent if needed is the proposed one-way text messaging.

The prototype is working as expected and can send a SMS to parent/guardian in case of emergency.

This system can be used by the TMS and be able to strengthen the policy of not bringing cell phone inside the campus. Students will have anytime readily mode of emergency communication through one-way text messaging system with their parent or guardian. This can be installed in several units around school strategically and serves as very good additional options to the TMS students.

Using RFID will enable students feel secured. Every student's RFID has unique card number and allow their RFID card to send SMS using the one-way text messaging system provided if they are registered to the system. The data base of registered students will control the access to be able to send SMS to student's registered number of parent/guardian. Also, There is no significant difference between the ECM and the regular cellular phone in terms of sending time. And there is a significant relationship between the sending time of the ECM and the number of characters sent.

5. RECOMMENDATIONS

The prototype made is intended to make the one-way text messaging system work like how to make



the RFID system function and be connected to raspberry pi, how the GSM system sends SMS without fail, and how these two systems collaborated using Java program. Here are the recommendations of the researchers to improve and optimize the system:

1. Upgrade the monitor to 7 inches for better reading and usage experience.
2. Change the RFID reader or module and GSM module to basic board function to lessen the cost of the system,
3. Find the same keyboard size that is easy to use.
4. Explore on using a smaller version of Raspberry Pi which is the Raspberry Pi Zero W model.
5. Design a container or box same size as the 7 inches monitor and RFID reader.
6. Install power bank module that can supply all power requirements of raspberry pi, RFID system, and GSM system.
7. Improve the cooling system to avoid excessive heat accumulating on the container.
8. Optimize the window (GUI) settings that can fit a 7inche screen.
9. Another thorough programming debugging to check possible bugs that will affect the sending of SMS and reading RFID performance.
10. Explore of using GSM modem instead of GSM module. This will enable two or more units share the same number. This is also a cost-effective approach.

- Morallo, I. M. (2015). Lyceum Of The Philippines University – Laguna Student Electronic Attendance And Logging System (Lpu-Laguna Seals). *Laguna Journal of Multidisciplinary Research*, 4(3), 1–1. <https://ejournals.ph/article.php?id=10049>
- Scanlan, D. A. (2015). An inexpensive RFID attendance system. | *Journal of Computing Sciences in Colleges. Journal of Computing Sciences in Colleges.* <https://dl.acm.org/doi/10.5555/1629036.1629039>

6. ACKNOWLEDGEMENTS

The researcher would like to thank everyone who helped them out in doing the project especially our adviser, Mr. John Henry P. Taguines.

The researcher would also like to thank their parents for supporting them in all the tasks to accomplish.

The researcher would like to thank Mr. Mark Espiritu for giving them his time to help make the program of the text messaging system.

The researcher would like to thank their school directress, Dr. Elizabeth T. Asiaten for trusting them to use the school's resources for their project.

And the One who made it all possible, THE ALMIGHTY GOD, for giving them confidence, courage, perseverance and knowledge to be an instrument for others' transformation.

7. REFERENCES

- Ban on use of cell phones during classes gets legislators' support. (2009, June 21). *Philstar.com*; *Philstar.com*. <https://www.philstar.com/cebu-news/2009/06/22/479599/ban-use-cell-phones-during-classes-gets-legislators-support>



Conceptualization of a Surveillance Drone for Aquatic Expeditions

Alfaro, Jio Jose G., Borbon, Kenneth A., and Tacbian, Kristian Rome L.
De La Salle University Integrated School, Manila

Dr. Alvin Y. Chua, *Adviser*; and Engr. Arvin H. Fernando, *Adviser*
De La Salle University, Manila

Abstract: The age of technology has paved the way for technological advancements and inventions, one of which are Unmanned Underwater Vehicles (UUV) which are deployed in marine ecosystems for various purposes. This technology displays the potential of safer and more efficient monitoring methods for marine surveillance. However, in the Philippines, numerous leading marine organizations still use traditional methods such as the use of divers to collect data for research purposes. Thus, it is the study's general objective to conceptualize a UUV model that may be adapted in the Philippines for marine surveillance operations. The study undergoes a 4-step process in fulfilling the general objective, this involves: (1) the Consultation of Marine Organizations and Personnel, (2) the finding of the Electrical Hardware Components, (3) the Simulation of the Conceptualized Drone Shapes, and (4) the Analysis of the Simulation Results. Through this systematic approach, the study conceptualized 3 drone shapes namely: the Disc Shape, the Torpedo Shape, and the Anomalous Shape. These conceptualized shapes were modeled and simulated through SolidWorks, where the ideal water conditions of the Philippines were set to accurately test the efficiency of these drone shapes. The obtained results suggest that the torpedo shape is the most ideal shape to utilize in Philippine marine surveillance application.

Key Words: unmanned underwater vehicle; conceptualize; SolidWorks; marine surveillance; drone shapes

1. INTRODUCTION

The UUV industry has introduced the viability of UUVs for marine surveillance. The integration of this drone technology underwater can be crucial in aiding long-term inexpensive, more task efficient, and safer practices in conducting underwater expeditions (The Explorer, n.d.). An example would be Irobot's Seaglider, a UUV specifically for surveillance purposes, that displayed the potential of UUVs for a safer and more efficient oceanic monitoring. However, given the diversities in the conditions of the world's bodies of waters, it is necessary to appropriate the drone design with regards to its own environmental challenges. As such, there is a surplus of different UUV designs in the market such as the spherical, torpedo, and anomalous each having their own sets of advantages and disadvantages (Chen & Liu, 2011).

The objective of this study is to conceptualize UUV models that may be adapted in the Philippines for surveillance purposes. The following steps were performed to accomplish the said objective:

1. To consult with various marine related organizations and personnel regarding various information needed for an ideal UUV.

2. To find the different electrical hardware components of the drone.
3. To simulate the hydrodynamics effects of different drone shapes through SolidWorks Flow Simulation.
4. To analyze the results of the simulation and identify the ideal drone shape to use in the Philippines.

The study aims to help various organizations in the Philippines that advocate towards the preservation of marine wildlife and coral reefs as the study conceptualizes UUV models that can be integrated in the Philippines. Furthermore, the study extends knowledge in the field of underwater drones as the study provides comparative data between different shapes of UUVs through the parameters coefficient of drag and drag force.

The primary focus of this study revolves around the effectiveness of various UUV shapes in Philippine oceans. The design aspect of the conceptualized drones relies on the incorporation of the various electrical components specialized for marine surveillance into the different hull shapes. Certain external procedures such as the programming

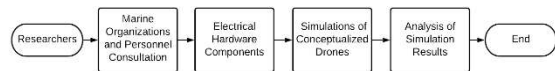


of the electrical components, actual fabrication of the drones, and post processing of gathered data by the drone is not included in the study. A total of 3 drone shapes were done in SolidWorks: spherical shape, torpedo shape, and manta ray shape. These designs were then tested through SolidWorks Flow simulation to identify their coefficient of drag and drag force.

2. METHODOLOGY

Figure 1

Flow of Methodology



Note. This figure shows the flow of which the objectives were done in sequence.

2.1 Marine Organizations and Personnel Consultation

Following the process seen in figure 1, proper guidance was imperative in setting the groundwork for the study to build upon. A survey was made through Google forms and was administered to various organizations and personnel in the field of marine biology. Personnel from marine organizations such as DLSU SHORE, Coral Guardian, Marine Conservation Ph, and National Oceanic and Atmospheric Administration (NOAA) took part in the survey; which includes inquiries about the ideal specs of an effective UUV while also including questions regarding the respondents' preferred drone shape based on the researchers' 3 initial drafts: the disc, the torpedo, and the manta ray (see Appendix A).

2.2 Electrical Hardware Components

The types of electrical components for the internal and external parts of the drone were selected to accommodate the compiled responses from the survey. The components to be included were centered around features, compatibility, and market availability. The various components were then compiled together in a table presenting their function, weight, quantity, and price (see Appendix B).

2.3 Simulations of Conceptualized Drone

2.3.1 Design Model

The 3 shapes in this subsection were modeled in SolidWorks by the researchers themselves. Every shape consists of the same components in quantity and quality but differs in its placement for each drone. Therefore, the shapes have been designed based on being compact with regards to the volume of the internal components. All of the designs were uniformly made out of 6061 aluminum alloy due to its

reliability in UUV applications. This material is popular in underwater applications as it is corrosive resistant and precipitation hardened (Metal Supermarkets, 2017). A tether was also integrated into the designs since radio waves cannot travel too well through water.

Table 1

Compiled Drone Models

Disc	Manta Ray	Torpedo
		

Note. This table presents the processed models through the use of SolidWorks Visualize for a more presentable look. This however does not change the overall shape and performance of the drones.

To model the disc shape seen in table 1, it was divided into two areas: the main component area and the outer ring area. To achieve this disc shape, 4 thrusters were mounted vertically along the x-axis of the outer ring area at an equal distance from one another. The concept behind the positioning of these thrusters is based on the thrusters of quadcopters. The outer ring area is connected to the main component area through the use of watertight enclosures that also functions as a means for the wiring of the thrusters to be safely connected to the main component area. The main component area comprises the electrical components necessary for the drone to function. Located on the side of the main component area is the pH sensor while below it is the mounted camera, temperature sensor, and depth pressure sensor. The 2 Subsea lights are located separately; one is located directly at the top of the main component area, while the other is located directly below the main component area.

Now for the modeling of the manta ray shape in table 1, the position of the thrusters is as follows: 2 thrusters mounted vertically for upward and downward motions, and 2 thrusters mounted horizontally for propelling the drone forward. Although the thrusters are mounted at different orientations, the thrusters were however aligned at the same axis with each other for them to function as intended. This is done in order for the drone to have stability while thrusting the drone forward. However, due to the 2 thrusters positioned at the back, a hollow passage was implemented in order for them to have access to water flow. For the other external components of the drone, the water quality sensors are allocated on a chin compartment below the hull; While




the internal components, the camera, and the two subsea lights are located inside the hull.

For the last design in table 1, the torpedo shape, there are 4 thrusters that are all positioned equidistant to each other located at the back of the drone where it can propel the drone forward. The other external components of the drone such as the water quality sensors and tether are also positioned in the back, while the camera and the subsea lights are allocated inside a chin compartment below the craft so that graphical recording is directed frontside of the drone's axis.

2.3.2 Actual Simulations

To set up the simulation environment, the following options were selected from the wizard command: external analysis excluding all cavities and internal spaces for the analysis type, water with a density of 1,023.6 kg/m³ for the fluid to be considered, and default for the wall conditions. According to Sea temperature (n.d.), the lowest recorded water temperature in Manila for the past years is 25°C with a corresponding density of 1,023.6 kg/m³. Due to the inverse proportion of temperature and density, using this temperature is tantamount to simulating the drones at the highest density. Now for the initial velocity condition, this was set to 1.5 m/s and 2.0 m/s derived from other drones that were considered (see Appendix C). However, due to the disc shape's design, two (2) assumptions were made in terms of how the initial velocity condition should be directed based on how it should be moving. First, if the thrusters can tilt, then the drone's movement should be parallel to the x-axis. Second, if the thrusters are fixed in its orientation, then the drone's movement should be approximately around 45° from the x-axis. The mesh settings used in the simulations can be seen in table 2 wherein these were set to: initial mesh level of 4, refining fluid cells level of 3, and refining cells at fluid/solid boundary level of 4.

Table 2
Mesh of the Drone Models

Disc	Manta Ray	Torpedo
		

2.4 Analysis of Simulation Results

The effectiveness of each UUV shape was based on the parameters: coefficient of drag and drag force. Thus, it was imperative to analyze the said

parameters in conjunction to the pressure contours and velocity flows. The analysis of the parameters was done via comparison and transparency checking with regards to present-day data. Important concepts such as the reference area and streamlined bodies were also considered in the analysis.

3. RESULTS AND DISCUSSION

3.1 MARINE ORGANIZATIONS AND PERSONNEL CONSULTATION

Table 3
Responses from the Consultation

Marine Organization/ Personnel	Recommended Electrical Hardware	Recommended Battery Duration	Recommended Operational Depth	Preferred Drone Shape
Director of DLSU Shore	Temperature Sensor	2 to 3 hours	50 meters	Spherical
Marine Ecologist of NOAA	Alkalinity Sensor Temperature Sensor	3 to 4 hours	30 to 50 meters	Torpedo
Marine Conservation Ph	pH Sensor Temperature Sensor	2 to 3 hours	40 or 150 meters	Torpedo
Coral Guardian	pH Sensor Temperature Sensor	2 to 3 hours	Purpose Dependent	Spherical

Note. Presented in this table are the summarized responses that were considered by the researchers in conceptualizing the disc, torpedo, and manta ray shapes.

3.2 Conceptualized Drone Simulations

Table 4
Compiled Simulation Results

Simulation Results at 1.5 m/s		
Drone Shape	Coefficient of Drag	Drag Force
Disc at 0°	-0.5585	-36.05
Disc at 45°	-0.1318	-49.31
Manta Ray	-0.4576	-27.63
Torpedo	-0.7927	-16.49
Simulation Results at 2.0 m/s		
Disc at 0°	-0.5596	-64.20
Disc at 45°	-0.1273	-84.69
Manta Ray	-0.4790	-51.42
Torpedo	-0.7928	-29.33

Figure 2
Coefficient of Drag vs Velocity

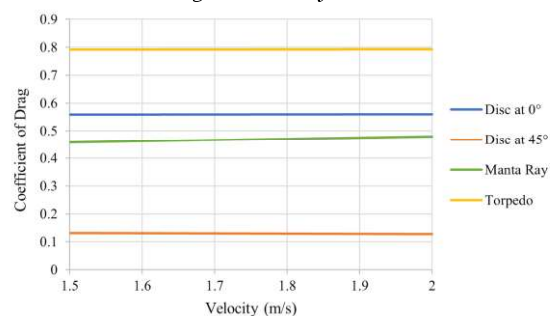


Figure 3
Drag Force vs Velocity

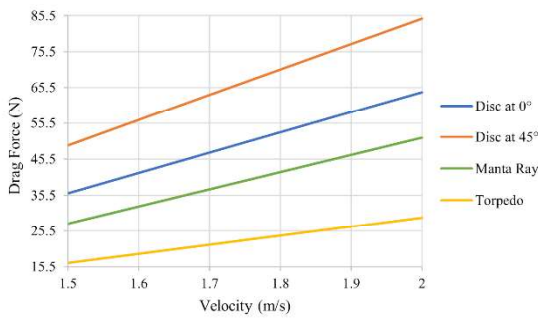
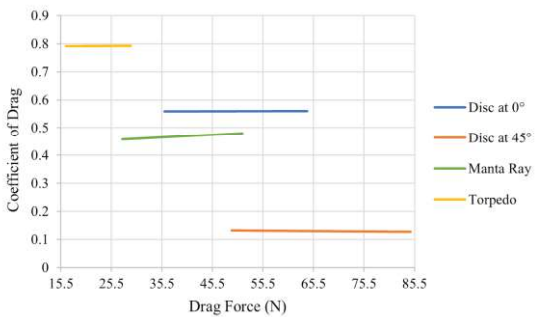


Figure 4
Coefficient of Drag vs Drag Force



As presented in figure 2, it can be noticed that among the 3 shapes, the disc shape at its second assumption, when it is angled at 45° from the x-axis, had the lowest coefficient of drag. An explanation to this is that among the factors that affect the drag equation, the reference area has an inverse relationship to the coefficient of drag (NASA, n.d.). This means that as the reference area increases, the coefficient of drag should decrease. Consequently, the disc at its second assumption had the least coefficient of drag while having the largest reference area among the other shapes as seen in table 5. This is consistent with the result obtained from the torpedo wherein the torpedo shape, which has the smallest reference area, had the highest coefficient of drag.

However, the coefficient of drag is not the sole determinant in the drag equation. According to Restarts (n.d.), drag force, the force obtained in the drag equation, is dependent on numerous other variables such as density, velocity, and shape. This explains the data seen on figure 3 wherein the disc at its second assumption yielded the highest drag force despite it having the lowest coefficient of drag. The reason behind its high drag force attributes to the flow of fluid with regards to its shape. Referring to table 6, it can be observed that heavy turbulence is experienced at the rear of the drone. In contrast to this, the torpedo shape experienced a more streamline flow of fluid that correlates to less agitation or

turbulence of fluid particles as it moves through a body (Swan, 2011). This resulted in a lower drag force despite its higher coefficient of drag.

Table 5
Compiled Pressure Contour

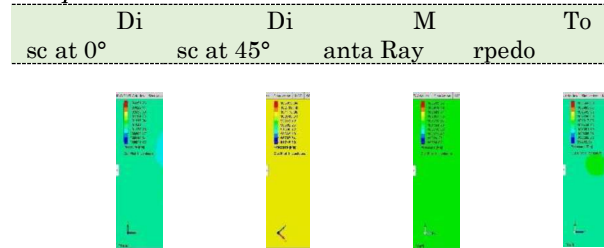
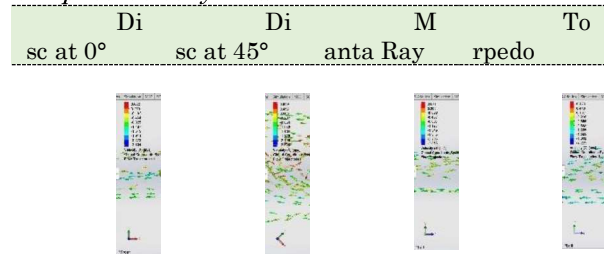


Table 6
Compiled Velocity Flow



4. CONCLUSION

This study, which aims to develop UUV models that can be adapted in the Philippines, has found out that based on the survey conducted, an ideal UUV should have 3 hours operational time and a depth rating of at least 30 meters. Moreover, the disc and torpedo shapes are preferred drone shape amongst the survey respondents. Now referring to the results seen in table 3, it can be inferred that based on the discussion in section 3, the ideal drone shape for the Philippines would be the torpedo. There were 2 bases for this interference. First, despite the torpedo's coefficient of drag being the highest, it was the closest one to the acceptable coefficient of drag value for underwater purposes. The coefficient of drag for most vehicles based on the cross-sectional area ranges from 0.8 to 1 (Marine Technology Society, 2017). Furthermore, the torpedo shape obtained the lowest drag force amongst the other drone designs. A similar observation was made in the thesis of Shah (2008) wherein he stated that torpedo shapes experience less drag compared to that of non-torpedo shapes.

For the proceeding studies to be conducted, a possible area of improvement for this research would be to consider upward and downward motions as well to investigate the lift force of the shapes. Moreover, simulation software that uses tetrahedral meshes such as Ansys could also be used to further improve the study as the SolidWorks Flow Simulation was only



limited to cuboid meshes. Lastly, a significant rendition of this study would be to fabricate the drones for actual experimentations.

5. ACKNOWLEDGEMENTS

The researchers wish to extend their sincerest gratitude to their families, research advisers, partners, survey respondents, and peers. The study was completed in recognition to the major contributions of guiding mentors namely; Dr. Alvin Chua, our research adviser, for guiding us towards the right trajectory; Engr. Arvin Fernando, our research adviser, for assisting us in completing the study; Engr. Isidro Marfori, our SolidWorks adviser, for aiding us in learning SolidWorks; Engr. Jeremias Gonzaga, the DLSU SolidWorks Coordinator, for lending us a licensed copy of SolidWorks Flow simulation. The researchers also recognize the significance of the study's survey respondents which set the groundwork for the study to stand upon. These contributions together with the perseverance of the researchers has enabled them to complete the study whilst imparting with them an unforgettable experience.

6. REFERENCES

Chen, Q., & Liu, J. (2011). Analysis of shape and general arrangement for a UUV. *Journal of Marine Science and Application*, 10, (1), 121-126. doi:10.1007/s11804-011-1051-8

Marine Technology Society. (2017). ROV APPLICATIONS-DESIGN-DRAG. https://web.archive.org/web/20190921045058/http://rov.org/rov_design_drag.cfm

Metal Supermarkets. (2017). Marine Grade Metals. <https://www.metalsupermarkets.com/marine-grade-metals/>

Nasa. (n.d.). The Drag Coefficient. <https://www.grc.nasa.gov/www/k-12/airplane/dragco.html>

Restarts. (n.d.). The Drag Equation. <https://www.fp7-restarts.eu/index.php/home/root/state-of-the-art/objectives/2012-02-15-11-58-37/132-drag.html>

Sea temperature. (n.d.). Sea water temperature in Manila today. <https://seatemperature.net/current/philippines/manila-sea-temperature>

Shah, V. (2008). Design considerations for engineering Autonomous Underwater Vehicles (Master's thesis, Massachusetts Institute of Technology). https://www.researchgate.net/publication/38000346_Design_considerations_for_engineering_Autonomous_Underwater_Vehicles

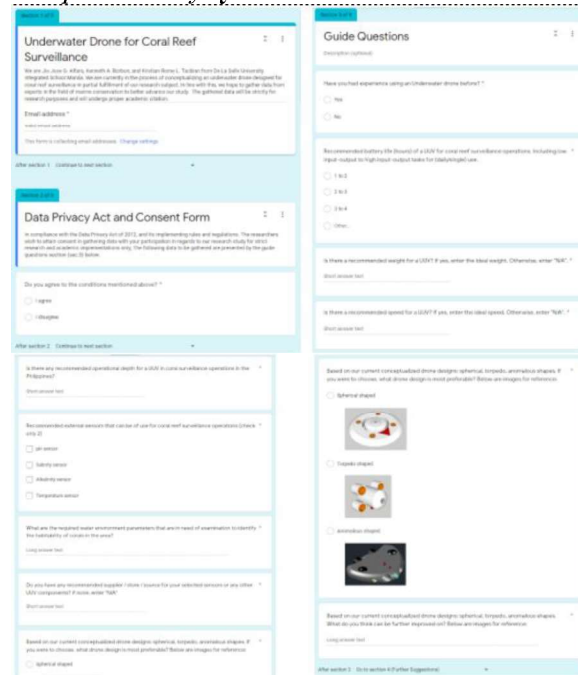
Swan, C. (2011). Streamline Flow. *Thermopedia*. doi: 10.1615/AtoZ.s.streamline_flow

The Explorer. (n.d). Underwater drones for ocean inspection and exploration. <https://www.theexplorer.no/solutions/underwater-drones-for-ocean-inspection-and-exploration/>

7. APPENDICES

Appendix A Survey Questionnaire

Figure A1
Compiled Survey Questionnaire



Appendix B Electrical Hardware Components Table B1

Internal Electrical Hardware Components

Component	Function	Weight	Quantity	Total Price
Pixhawk Autopilot	An advanced autopilot/command center through which each command is taken and translated to the other components of the drone	33.3 grams	1	\$170.00
ZTW 40A Brushless ESC	A non-physical controller that indicates the speed of the thrusters' speed.	36 grams	4	\$72.00
BlueRobotic Power Sense Module	A module that provides current and voltage sensing to the Pixhawk autopilot	Not indicated	1	\$31.00
Fathom-x Tether Interface Board Set	A tether interface board that Enables HD video and high-bandwidth data over 300m+ tether lengths.	N/A	2	\$338.00
Raspberry Pi 3 Model B+	A credit-card sized computer with a 1.4GHz 64-bit quad-core processor, dual-	45 grams	1	\$48.00



3RD DLSU SENIOR HIGH SCHOOL RESEARCH CONGRESS

COMPUTER AND SOFTWARE TECHNOLOGY, AND ROBOTICS

	band wireless LAN, Bluetooth 4.2/BLE, faster Ethernet, and Power-over-Ethernet support			
BlueRobotic 16 GB SD card preloaded with Raspian for ArduSub	A micro SD card preloaded with the Raspbian Linux Operating system and is preloaded with the software needed for ArduSub	Not indicated	1	\$16.00
BlueRobotic Left-Angle Micro USB Cable for Raspberry Pi to Pixhawk	A cable capable of connecting a Micro-USB to USB-A cable which can be connected to the Raspberry Pi computer and Pixhawk autopilot	23 grams	1	\$10.00
BlueRobotic 5V 6A Power Supply	A simple voltage regulator that provides a steady 5V at up to 6A for Raspberry Pi and Pixhawk servo rail.	Not indicated	1	\$22.00
HiLetgo MPU9250 Gyroscope, accelerometer, magnetometer sensor	A powerful inertial measurement unit (IMU) for Raspberry Pi 2/3/4 that adds X, Y, Z axis-functions for determining acceleration, and magnetometer sensor.	2.72 grams	1	\$8.99
Battery	A custom-made battery-pack that accommodates the required electrical output of the 4 thrusters and other components	Not indicated	1	

Table B2
External Electrical Hardware Components

Component	Function	Weight	Quantity	Price
GAOHAU pH 0-14	An underwater pH sensor with a pH range of 0-14 pH and <= 1 minute.	136.078 grams	1	\$40.99
BlueRobotics Celsius Fast-Response, ±0.1°C Temperature Sensor (I2C)	An underwater temperature sensor has an accurate sensor of down to tenths-celsius and a fast response/reading time of (0.5 m/s flow).	Not indicated	1	\$60.00
BlueRobotics Bar30 High-Resolution 300m Depth/Pressure Sensor	An underwater pressure sensor for 300m depth operating capacity and depth resolution of 2mm.	Not indicated	1	\$72.00

BlueRobotics Low-light HD USB Camera	An underwater camera based on the Sony IMX322 with a 1/2.9" sensor and a 2MP-1080p pixel count: to attain maximum light sensitivity.	Not indicated	1	\$99.00
BlueRobotics Lumen Subsea Light	An underwater observation light with a fully dimmable PWM and has a light efficiency output of 1500 lumens at 15 watts. Its beam is rated with a 135° coverage and 6200k color temperature.	Not indicated	1	\$115.00
Hawk Hobby Underwater Thrusters	An underwater reversible thruster with 860 RPM and rated at 300W max power.	163 grams	1	\$49.99
Camera Mount	A custom-built 3D CAD camera mount for the BlueRobotic Low-light HD USB Camera	Not indicated	1	Not applicable
Fathom ROV Tether	A 70-meter polyurethane jacketed tether connected to the drone's tether interface board which connects the drone to the topside computer.	Not indicated	1	\$350.00
Microsoft Xbox One Controller	A wired/wireless gamepad controller is compatible with Windows 10 or Linux operating systems.	281 grams	1	\$59.99
Topside Computer	A topside Windows 10 os operating device with 8GB ram, i5 processor, and	Not indicated	1	649\$



	solid-state drive (SSD).			
--	--------------------------	--	--	--

Appendix C
Research and Commercial Drone Specifications
Table C1

Available Drone Specifications

Disc Drones				
Drone	Max Speed	Battery Duration	Battery Capacity	Max Depth
Kiro Developed Drone	2.1 m/s	Not indicated	Not indicated	Not indicated
Underwater Disk Robot	2.57 m/s	Not indicated	3000W	Not indicated
Spherical Auv	Not indicated	Not indicated	8kWh	150 meters
Four Rotor Dish Drone	Not indicated	Not indicated	Not indicated	Not indicated
Torpedo Drones				
Bluefin-21	2.3 m/s	Not indicated	13.5 kWh	4500 meters
SPURV	1.95 m/s	5 hours	Not indicated	3650 meters
REMUS-100	2.6 m/s	Not indicated	1.5 kWh	100 meters
Anomalous/Commercial Drones				
PowerDolphin	4.5 m/s	2.0 hours	5,800 mAh	Not indicated
iBubble	1.5 m/s	1.5 hours	Not indicated	60 meters
Fifish V6	1.5m/s	4 hours	9000 mAh	100 meters
Gladius Mini	2.0 m/s	2 hours	5000 mAh	100 meters
Blueye Pioneer	1.5m/s	2 hours	96 Wh	150 meters